N95-27630

An Overview of the Evaluation of Oxygen Interactions with Materials III Experiment: Space Shuttle Mission 46, July-August 1992.

Steven L. Koontz, Lubert J. Leger, James T. Visentine; NASA Johnson Space Center, Houston, TX, 77058, (713)-483-8916

Don E. Hunton, USAF Phillips Laboratory, Hanscomb Air Force Base, MA, 01731, (617)-377-4057

Jon B.Cross, Los Alamos National Laboratory, CS2, J-565, Los Alamos, NM., 87545, (505)-667-0511

Charles L. Hakes, Lockheed Engineering & Sciences Company, Houston, TX, 77058, (713)-333-7804

ABSTRACT

The Evaluation of Oxygen Interactions with Materials III (EOIM-III) flight experiment was developed to obtain benchmark atomic oxygen reactivity data and was conducted during Space Transportation System Mission 46 (STS-46), July 31 to August 7, 1992. In this paper, we present an overview of EOIM-III and the results of the Lyndon B. Johnson Space Center (JSC) materials reactivity and mass spectrometer/carousel experiments. Mass spectrometer calibration methods are discussed briefly, as a prelude to a detailed discussion of the mass spectrometric results produced during STS-46. Mass spectrometric measurements of ambient O-atom flux and fluence are in good agreement with the values calculated using the MSIS-86 model of the thermosphere as well as estimates based on the extent of O-atom reaction with Kapton polyimide. Mass spectrometric measurements of gaseous products formed by O-atom reaction with C^{13} labeled Kapton revealed CO, CO_2, H_2O, NO and NO_2. Finally, by operating the mass spectrometer so as to detect naturally occurring ionospheric species, we characterized the ambient ionosphere at various times during EOIM-III and detected the gaseous reaction products formed when ambient ions interacted with the C^{13} Kapton carousel sector. By direct comparison of the results of on-orbit O-atom exposures with those conducted in ground-based laboratory systems, which provide known O-atom fluences and translational energies, we have demonstrated the strong translational energy dependence of O-atom reactions with a variety of polymers. A "line-of-centers" reactive scattering model was shown to provide a reasonably accurate description of the translational energy dependence of polymer reactions with O atoms at high atom kinetic energies while a Beckerle-Ceyer model provided an accurate description of O-atom reactivity over a three order-of-magnitude range in translational energy and a four order-of-magnitude range in reaction efficiency. Postflight studies of the polymer samples by x-ray photoelectron spectroscopy and infrared spectroscopy demonstrate that O-atom attack is confined to the near-surface region of the sample, i.e. within 50 to 100 Angstroms of the surface.

INTRODUCTION

Oxygen atoms are the most abundant neutral constituents of the Earth's ionosphere at altitudes ranging from 200 to 700 km[refs 1-3] and have been shown to be one of the more important environmental factors involved in the degradation of several important classes of spacecraft materials[ref 4,5]. The primary objective of the EOIM-III experiment was to produce benchmark atomic oxygen reactivity data for a wide range of materials[ref 6]. Secondary objectives included: 1) mass spectrometric characterization of the gaseous reaction and scattering products formed when the ambient atmosphere interacts with various materials, 2) characterizing the induced environment produced by interaction of the ambient atmosphere with the EOIM-III experiment and the Space Shuttle cargo bay, and 3) characterizing the chemical reaction dynamics of the reaction between O-atoms and polymers. In this paper, we present an overview of the EOIM-III experiment as performed during STS-46 during early August 1993. EOIM-III was a team effort with coinvestigators from all major NASA field centers, the United States Air Force, the European, Japanese and Canadian space agencies and the Ballistic Missile Defense Office.

Our approach to achieving EOIM-III objectives was based on comparing measurements of materials samples after exposure to known O-atom fluences in three well-characterized environments: 1) The low-Earth-Orbit (LEO) environment, 2) the high-velocity neutral-atom beam (HVAB) system at the Los Alamos National Laboratory (LANL), and 3) a flowing discharge or downstream plasma system at JSC. Detailed characterization of the exposure environments was accomplished by determining such factors as O-atom flux and fluence as well as O-atom kinetic energy distribution function, sample temperature, ultraviolet/vacuum ultraviolet (UV/VUV) radiation dose and surface contamination.

The methods and results of the EOIM-III environment characterization effort are described in detail in the accompanying paper[ref 1]. Briefly, the atomic oxygen fluence was determined by calculation using the MSIS-86 model of the thermosphere combined with as flown trajectory and vehicle attitude data[ref 7] as well as daily average values (24-hours average) of the solar activity indices. A second estimate of the O-atom fluence was obtained from direct measurements of the O-atom flux using a mass spectrometer[ref 8] provided by the USAF Phillips Laboratory[ref 9]. Kapton polymer film standards were also used to obtain an additional estimate of O-atom fluence by simply measuring mass loss and surface recession after the mission and using the widely-accepted value of $3.0 \times 10^{-24} cm^3$/atom[ref 10] as the Kapton reaction efficiency.

The thermal history of the payload was recorded with an array of thermocouple sensors[ref 1], and the solar UV/VUV dose was estimated using daily average solar flux data from the Upper Atmosphere Research Satellite[ref 1] combined with a detailed analysis of the Space Shuttle attitude history. Payload contamination was evaluated by post flight X-ray photoelectron spectroscopy of selected samples and monitored during

the mission with an array of Temperature Controlled Quartz Crystal Microbalances (TQCMs)[ref 1].

EOIM-III Flight Experiment: Description and Performance

The EOIM-III flight hardware is briefly described below. Photographs of the EOIM-III payload, after installation in the Space Shuttle Atlantis and removal of protective covers, are shown in figure 1 . A line drawing of EOIM-III identifying the various sub-assemblies and experiments is shown in figure 2 and can be used to identify the various features shown in figure 1. The overall cargo bay layout of STS-46 is shown in figure 3. EOIM-III was mounted on a Multipurpose Payload and Experiment Support Structure ("MPESS" structure), on the starboard side of the Space Shuttle Atlantis, near the aft bulkhead, and at the level of the orbiter sill longeron, i.e., at the level of the cargo bay door hinge line. The carousel and mass spectrometer are visible in the middle of the EOIM-III pallet, with the passive sample carriers on the outboard side and the heated trays and environmental monitor package inboard, toward the center of the Space Shuttle cargo bay. In figure 1 the mass spectrometer is pointed along the cargo bay normal (-Z in orbiter coordinates) and the motorized lid is closed. The mass spectrometer ion source was of the semi-open variety as defined by Hayden, Neir, et al.,[ref 11] and was capable of receiving neutral gas from a 180-degree field of view. Only the vertical stabilizer, several cargo bay components including the aft bulkhead, and the orbital manuvering system pods are line-of-sight to the mass spectrometer ion source (although only occupying a small, perifieral fraction of the field of view) and, by implication, the rest of the payload[ref 1]. A cross sectional drawing of the mass spectrometer is shown in figure 4.

The as-flown altitude and attitude timelines for STS-46 are shown in figures 5 and 6. The attitude timeline shows the angle between the cargo bay normal (-Z in orbiter coordinates) and the orbiter velocity vector. The angle shown in figure 6 runs from 0 degrees, corresponding to the -ZVV or ram orientation, to 180 degrees, corresponding to ZVV or antiram (heat shield into the velocity vector). The oscillations between 0 and 180 degrees visible during earlier parts of the mission correspond to inertial hold attitudes or roll maneuvers. The orbital inclination was 28.5 degrees and the beta angle (the angle between the Sun pointing vector and the plane of the Space Shuttle orbit) varied between 17.5 and 24.3 degrees. EOIM-III was initiated at Mission Elapsed Time (MET) 5 days, 22 hours, 30 minutes (5:22:30 = 142.5 hrs.), shortly after reducing orbital altitude to 123-124 nmi. A waste-water dump was conducted between MET 5:20:37 and MET 5:22:30 with the orbiter attitude adjusted to minimize the chance of particles from the waste stream recontacting the orbiter. The orbiter was placed in the -ZVV attitude for EOIM-III at MET = 142.5 hrs.

In general, the EOIM-III flight hardware performed well during the mission. Primary electric power was applied to the payload at MET 0:3:22 and telemetry was then enabled. Before EOIM-III was initiated, the mass spectrometer was operated only as

needed in order to obtain natural and induced environment data for selected vehicle attitudes and operations. The mass spectrometer was pointed in the -Z direction, as shown in figures 1 and 2, throughout the pre EOIM-III portion of the mission and operated so as to alternately collect mass spectra of neutral gases (the electron impact ionization filaments and a repeller grid to exclude ambient ions were both powered on) in neutral mode, or ambient ions (filaments and repeller grid off) in ion mode during alternating 1 minute intervals. In addition, payload temperature data were recorded throughout the mission using thermocouples placed as described in the accompanying mission and induced environments paper[ref 1].

After initiation of the EOIM-III experiment, the EOIM-III payload executed a series of timed operating cycles in which mass spectrometric measurements of the ambient atmosphere and ionospheric constituents alternated with mass spectrometric measurements of reaction and scattering products formed when ambient species interacted with various carousel sectors each of which was coated with one of the following materials: 1) C^{13} labeled Kapton polyimide prepared by the Jet Propulsion Laboratory; 2) anodized aluminum; 3) Chemglaze Z-306 black polyurethane based space paint; 4) FEP Teflon, 5) Parylene-C coated stainless steel. The carousel sectors were designed so that the geometric field of view of the mass spectrometer ion source contained only carousel sector surfaces. A movable carousel sector cover blocked direct incidence of atmospheric species during a portion of each carousel sector observation period so that the induced environment from both direct ram and scattered ram could be measured.

In addition to carousel/mass spectrometer operations, heated tray temperatures were established at 60, 120 and 200 degrees Centigrade (prior to placing the orbiter in the ram -ZVV attitude for EOIM-III) and timed sample tray cover movements for the variable exposure trays (VET) and solar ultraviolet (SUV) trays were initiated. The VET cover failed to operate correctly, and all sample specimens received the same nominal O-atom fluence. The SUV and heated tray experiments operated properly. Two payload-switching problems were encountered which have not been explained to date. First, the mass spectrometer did not respond to a power-off command leading to 13.6 hours of unplanned operation early in the mission. Second, the preprogrammed mass spectrometer/carousel cycle did not initiate properly on the first try so that the carousel observations were delayed by about 6 hours. Despite the switching problem, neutral mode mass spectra were obtained for all carousel segments and ion mode spectra were obtained for the Z-306 and the C^{13} labeled sectors.

The reactivities of EOIM-III polymer samples were determined by two complementary methods: 1) weight loss and 2) profilometry. In most cases, two disk samples of each polymer were placed in each sample holder opening. The top sample was directly exposed to the space environment and interacted with atomic oxygen, UV/VUV radiation and other space environment factors while the underlying sample was exposed only to thermal vacuum. Both samples were subjected to high-vacuum baking and were weighed before and after the mission. Both samples were cleaned by rinsing

briefly with Q Clean[tm] Solvent, (Thermo Analytical Inc., Monrovia Calif.) an ultra-high-purity cleaning solvent, and were then air dried in a laminar flow hood prior to installation in the EOIM-III sample holders. Polymer film samples were tested for short-term compatibility with Q Clean[tm] before cleaning. The top sample was also covered with a high-transparency metal grid which acted as an etch mask. In this way, the well-known highly-directional nature of high-velocity O atom reactions with polymeric materials was exploited to advantage by producing a regular pattern of ridges on O-atom reactive polymers. The regular pattern of ridges produced with the etch mask makes profilometry more accurate in the presence of the natural surface irregularities always present on polymer film samples. All polymer film specimens were used as-received from the vendors except for the vacuum baking and cleaning process described above. However, the two liquid crystal polymers, Xydar and LCP-4100, were also polished because the surface roughness of the as-received material was too great to permit accurate profilometry even with use of the metal screen etch masks.

EOIM-III Laboratory Support Instrumentation: Apparatus and Methods

Laboratory measurements and calibrations were a key component of the EOIM-III experiment. Effects resulting from sample exposure to laboratory O-atom systems were compared to those resulting from on-orbit O-atom exposure to gain insight into reaction mechanism and to verify various approaches to ground-based testing. In addition, the EOIM-III mass spectrometer was calibrated in a ground-based, high-velocity O-atom beam system. Finally, most materials reactivity determinations were made by post exposure laboratory measurements of exposed specimens for comparison with controls. Weight loss, surface recession by profilometry, scanning electron microscope images, x-ray photoelectron spectroscopy, thermomechanical analysis, and transmission infrared spectroscopy were the most important sample characterization techniques used for the JSC samples. Two laboratory O-atom systems were used to provide comparison data: 1) the flowing discharge and 2) the HVAB. In general, polymer specimens were prepared as for flight on EOIM-III (see proceeding section). Polymers exposed to the HVAB beam were, however, bonded to aluminum heat sinks using a silicone-free epoxy cement so as to assure known sample surface temperatures despite heating by beam-source thermal radiation.

The methods and apparatus used to determine the O-atom reactivities of polymers in the flowing discharge (remote plasma) apparatus have been described[ref 12,13]. Briefly, a working gas (10% O_2/90%Ar), at total pressures on the order of 2 Torr, was passed through a 2.45 GHz Evenson discharge cell and flowed downstream from the discharge before coming into contact with the polymer samples so that the gas had cooled to room temperature but still contained oxygen atoms in the O^3P electronic ground state. The O-atom concentration was determined by chemiluminescent titration using NO_2[ref 14,15] and the atom flux on sample surfaces is determined using well-known methods for modeling flowing reaction-diffusion systems[ref 16]. Both the samples and the reactive gas could be heated to determine Arrhenius activation energies. Unlike the

atom beam and space flight experiment experiment, both of which deliver O-atoms to the polymer surface in the form of a directed beam, the flowing discharge delivers O-atoms to the polymer surface by diffusion from an isotropic gas in thermal equilibrium with the polymer sample. This does not necessarily imply that the comparison of flowing discharge and directed beam O-atom processes is invalid in an "apples and oranges" sense simply because the O-atom reaction with the sample surface still depends on an O-atom surface collision. In addition, the flux of molecular oxygen was much higher in the flowing discharge than in the LEO or HVAB environments described above, though large variations in O_2 partial pressure revealed no effects on the reactivity of Kapton, Mylar or polyethylene in the flowing discharge system[ref 13,16]. Polymer reactivity in this system was determined by periodically venting the system and weighing the polymer specimens on a six-place laboratory balance. The observed mass loss was always significantly greater than any water adsorption or desorption effects.

The HVAB has been described[ref 17,18]. Briefly, a laser-sustained gaseous discharge (50% O_2/Ar or O_2/Ne at pressures on the order of 2000 Torr) undergoes supersonic nozzle expansion to form a seeded beam of oxygen atoms (O^3P electronic ground state) and inert gas atoms. The average kinetic energy can be varied between 0.4 and 3 eV. Beam velocity distribution functions were determined directly using well-known time of flight (TOF), methods[ref 17,18] with phase-sensitive (modulated atom beam) mass spectrometric detection to reject vacuum system background. The mass spectrometer used for beam characterization was not the EOIM-III mass spectrometer but, rather, a component of the HVAB system.

The O-atom flux in the beam was determined using both relative abundance from the mass spectrometric measurements of beam composition using TOF methods and the pressure rise in an accommodation chamber (measured with a spinning rotor type pressure gauge and residual gas analyzer) as was previously reported[ref 9]. Given the inert gas flux in the beam and the relative abundances of the various high-velocity beam species from phase-sensitive mass spectrometry, the fluxes of all other beam species, including atomic oxygen, were calculated using known values of electron impact cross sections, the mass spectrometric transmission function, and the change in mass spectrometer sensitivity with atom or molecule velocity[ref 18]. The well characterized O-atom beam used for calibration and characterization of the EOIM-III flight mass spectrometer was also used to support polymer reaction efficiency measurements in this system.

The typical polymer film temperature during exposure to the O-atom beam was 45 degrees centigrade, and the samples could be heated to determine Arrhenius activation energies. Gaseous reaction products were detected using phase-sensitive (modulated beam) mass spectrometric detection techniques[ref18] to reject vacuum system background.

Results and Discussion of Results: Mass Spectrometer/Carousel

The mass spectrometer carousel system produced about 48,000 neutral and ion mass spectra during STS-46. Typical ram mass spectra taken: 1) during the post Eureca deployment ram orientation period (altitude = 430 km) and 2) at the beginning of the EOIM-III (altitude = 230 km) are shown in figures 7a and 7b, respectively. For comparison purposes, a typical mass spectrum produced during the calibration process at LANL is shown in figure 8. Atomic oxygen is visible at mass 16 in figures 7 and 8, with water at mass 18 and the OH^+ ion at mass 17. Molecular oxygen is visible at mass 32 in both figures and is formed by recombination of atomic oxygen in the mass spectrometer ion source (neither the HVAB beam nor the LEO environment contains significant amounts of O_2). The mass 40 and 20 peaks in figure 8 are form Ar^+ and Ar^{++} respectively. Figures 7 and 8 show a number of features not apparent in figure 18. The intense peak at mass 28 amu is produced by molecular nitrogen, a natural component of the atomophere at Shuttle operating altitudes, and the associated atomic nitrogen fragment is visible at mass 14. The mass peak at 44, with an associated doubly charged peak at 22, as well as an atomic carbon fragment peak at mass 12, is attributed to CO_2. The CO peak (mass 28) is obscured by the N_2 peak at mass 28. H_2O and CO_2 are not components of the natural environment at shuttle operating altitudes but can be produced by both active (O-atom reactions with cargo bay materials) and passive outgassing of space shuttle cargo bay components and the mass spectrometer itself. The low intensity mass peaks at 23 and 39 amu correspond to sodium and potassium, also not components of the natural environment, and have been reported in mass spectra produced by satellite borne instruments[ref 31].

The high-background current visible in the calibration spectrum (figure8) is the result of scattered UV/VUV radiation from the HVAB source which was coaxial with the ion flight path of the mass spectrometer. The same high background current would be visible in the EOIM-III mass spectra if the instrument had been directly facing the Sun, but the combination of orbital inclination, beta angle (the angle between the Sun vector the orbital plane), and vehicle attitude precluded that event during STS-46 (the 180^o field of view applies to the ion source only, not the complete path from ion source to secondary electron multiplier). During EOIM-III and the various HVAB calibration experiments, the mass spectrometric sensitivity decreased as a function of O-atom fluence. However, the O-atom fluence dependence of the mass spectrometer was different in the on-orbit and high velocity atom beam environments[ref 1].

Only a 30 percent loss of signal was noted in the photocurrent background at LANL while a factor of 6 decrease in ion current was noted under constant O-atom flux conditions. The effect of O-atom fluence on mass spectrometer sensitivity is believed to be due to the formation of gold oxide on the surfaces of the gold-plated ion source optics in the EOIM-III mass spectrometer. This effect was previously reported to occur during mass spectrometric sampling of ions form flowing discharges with gold sampling orifices[ref 19]. Formation of a dielectric layer on the ion optical elements

degrades the sampling efficiency of the ion source. Some degradation of secondary electron multiplier performance was observed via changes in the amplitude of the photocurrent background during high fluence calibration experiments at LANL; the effect is small compared to the observed mass spectral sensitivity loss. The formation of gold oxide (Au_2O_3) from gold and molecular oxygen is not observed because the process is endothermic at 19.3 kcal/mole. In contrast, the formation of gold oxide from gold and atomic oxygen is exothermic at -159 kcal/mole.

Finally, it is interesting to note that different O_2/O ratios were obtained on orbit and in the laboratory ($O_2/O = 2.8$ on orbit; $O_2/O = 1.5$ at LANL). Since O_2 constituted less than 3 percent of the high-velocity gas entering the mass spectrometer in both environments, the very different O_2/O ratios observed suggest that O-atom recombination and transport processes were following different kinetic laws in the two environments.

The immediate conclusion obtained from the comparison of mass spectrometric performance on orbit and in the laboratory is that simple direct application of the LANL calibration results to the on-orbit data will not give the best accuracy. O-atom fluence estimates based on mass spectrometric data range from 2.2×10^{20} to 4.7×10^{20} atoms per square centimeter depending on the approach we used in applying the calibration results to the on-orbit data. As of this writing, the mass spectrometric fluence estimate is $2.3 \pm 0.7 \times 10^{20}$ O atoms/cm^2. This fluence estimate was calculated as follows. First, the calibration factor at zero O-atom fluence is taken as 2.3×10^{23} (atoms/cm^2)/amp, as determined in the HVAB facility at LANL. The corrected mass16-peak areas (corrected by subtraction of 26 percent of the mass 32-peak area, 0.15 percent of the mass 18-peak area) are multiplied by the sensitivity decay function to correct for O-atom fluence dependent instrument sensitivity loss. The sensitivity decay function was obtained by fitting an exponential decay function to the on-orbit mass 16-peak area data (i.e. except for diurnal variations, the O-atom flux was assumed to be approximately constant). Finally, the corrected mass 16 peak areas were multiplied by the zero fluence calibration factor to obtain the O-atom flux. The flux is calculated at regular time intervals and summed to obtain the mass spectrometer O-atom fluence measurement for those time periods when the mass spectrometer was on and producing O-atom flux measurements. Division of the mass spectrometric fluence calculated above by the duty cycle, i.e. the fractional time on and measuring O-atom flux, gives the final value for the mass spectrometric O-atom fluence.

Typical mass spectra of the induced neutral environment in the C^{13} labeled Kapton carousel sector are shown in figures 9 (sector open to direct ram flux) and 10 (sector cover on blocking direct ram flux). Comparison with the typical ram mass spectra (figure 7) shows that scattered ambient species dominate the induced environment. Gaseous reaction products are a significant part of the spectra, however, and $C^{13}O_2$ and $C^{13}O$ are visible in figures 9 and 10. Gaseous reaction products formed during exposue of an identical C^{13} Kapton sample to the HVAB at LANL is compared with

EOIM-III measurements in figure 11 demonstrating that the same gaseous reaction products are produced in both environments. The higher levels of NO at mass 30 in flight is probably formed by environmental interaction processes not directly related to O-atom reactions with polymers. Mechanisms previously proposed to explain the visible spacecraft glow phenomena may explain the high NO signal observed[ref 30].

Moving the cover over the carousel sector produced little effect except for a net reduction in spectral intensity (figures 9&10). The fact that the sector cover had little effect is attributed to the scattering of ambient ram species from the EOIM-III pallet, near the opening to the carousel sector, as well as scattering of cargo bay induced environment gases from aft bulkhead surfaces. With the cover in position over the carousel sector, incomplete momentum accommodation (on surface collision) can result in relatively high kinetic energy (i.e., high reactivity) O atoms colliding with the carousel sample surfaces after only two reflections, one from the EOIM-III pallet and one from the sector cover surface which faces the sample compartment.

The EOIM-III mass spectrometer measured ions in the natural and induced environment when the electron impact ionizer and the repeller grid were turned off as described above. A typical ambient ion mass spectrum taken with the mass spectrometer ion source in a ram orientation during EOIM-III operations at a 230 km altitude is shown in figure 12. Mass spectra of the induced ionic environment, formed by interaction of naturally occurring ionospheric ions with the C^{13} Kapton carousel sector, are shown in figures 13 (sector cover off) and 14 (sector cover on). The difference between the ambient ram mass spectra and the induced environments spectra is more notable in this case than in the neutral case of figures 9 and 10. Isotope-labled reaction products are visible in the mass spectra of the Kapton carousel sector and may result either from direct reaction of O^+ ions with the carousel sector surfaces or gas phase charge exchange of O^+ ions with the gaseous reaction produced by neutral O-atom attack on the polymer. It is also interesting to note that in contrast with the induced neutral environment mass spectra of the same carousel sector, mass spectra of the induced ionic or plasma environments showed a dramatic decrease in intensity when the carousel sector cover moved into position showing that ionospheric plasma ions are efficiently neutralized during collisions with payload surfaces.

Results and Discussion: O-Atom Reactions with Polymeric Materials.

Polymer reaction efficiencies (cm^3 of material removed per incident O atom) determined following exposure on orbit in the EOIM-III passive trays, are shown in table 1, where EOIM-III measurements are compared with those made following previous flight experiments. The reaction efficiencies reported in table 1 were determined by weight loss only; the repeatability of the measurement is indicated as the difference between the largest and smallest measurement, if more than one sample was exposed on orbit. Comparison of the EOIM-III reaction efficiency column in table 1

with those of previous missions demonstrates that the polymer reaction efficiency data base has been both enlarged and verified.

Table 1. Polymer Reaction Efficiencies

POLYMER	Re (EOIM-III) x 10^{24}	Re (STS-8) x 10^{24}	Re (STS-41) x 10^{24}	Re LDEF x 10^{24}
KAPTON (LeRC R.R.)	3.1	3.0	3.3	3.0
EYMYD-F (ETHYL CORP.)	2.7			
CR-39 POLYCARBONATE	6.1	6.0		
PEEK (ICI)	3.4		4.3	
XYDAR (AMOCO)	2.9			
LCP-4100 (DuPont)	3.2			
MYLAR A (DuPont)	3.8	3.9		
POLYETHYLENE (PE)	4.4	3.7		
HDPE (PHILLIPS, EMH6606)	3.7	3.7	3.5	
POLYMETHYLPENTENE (PMP, MITSUI)	5.3			
POLYPROPYLENE	5.5		4.4	
TEDLAR (DuPont)	3.5	3.2		
TEFZEL (CLEAR, DuPont)	0.9		0.2	
TEFZEL (BLUE, RAYCHEM)	1.1			
TEFZEL (WHITE, RAYCHEM)	0.9			
KYNAR (PENWALT)	1.2			
KEL-F (PCTFE, 3M)	0.9			
HALAR (ALLIED)	1.9			
ACLAR 33C (ALLIED)	1.0			
FEP TEFLON (LeRC R.R.)	0.05	<0.03	<0.03	0.3
TFE TEFLON (DuPont)	0.06	<0.03		0.5
EYPEL-F, (ETHYL CORP.) POLY(BISTRIFLUOROPRO-PYLPHOSPHAZENE)	<0.03			

The results of replicate measurements of the reaction efficiency of Kapton polyimide demonstrate excellent agreement between the profilometry and weight loss measurements. Weight loss on four Kapton samples produced a reaction efficiency of $3.05 \pm 0.1 \times 10^{-24}$ cm^3/atom while profilometry of four different Kapton samples produced a reaction efficiency of $3.16 \pm 0.1 \times 10^{-24}$ cm^3/atom, using 2.3×10^{20} atoms/cm^2 as the fluence estimate. Both numbers are in excellent agreement with the Kapton reaction efficiencies produced by other on-orbit materials experiments such as STS-8[ref 21] (3×10^{-24}), the Long-Duration Exposure Facility[ref 22] (LDEF) (3.0×10^{-24}) and the Intelsat Solar Array Coupon (ISAC) experiment flown on STS-41[ref 5] (3.1×10^{-24}). The HVAB at LANL was used to produce an independent (independent of MSIS-86 calculations) estimate of the Kapton reaction efficiency as

described below. The value of the Kapton reaction efficiency determined in the HVAB is 3.3×10^{-24}, within 10 percent of the values produced by the flight experiments.

Several general trends in the relationship between O-atom reactivity and molecular structure are visible in table 1. For example, polyethylene,Tedlar, Tefzel, Kynar and Teflon are all linear carbon chain polymers with increasing fluorine content and decreasing hydrogen content as we move along the series from polyethylene, $(CH_2\text{-}CH_2)_n$, or polypropylene, to Teflon, $(CF_2\text{-}CF_2)_n$, or FEP Teflon. As can be seen in table 1, increasing fluorine content results in decreasing O-atom reaction efficiency, as we would expect if hydrogen atom abstraction is a rate-limiting process and fluorine atom abstraction occurs to a very limited extent, if at all. The EOIM-III reaction efficiency for Teflon is intermediate between that reported from STS-8[ref 20] and LDEF[ref 21]. We attribute the observed range of reaction efficiency values to different net doses of solar UV/VUV radiation in the different mission environments. Vacuum ultraviolet photochemistry has been shown to be the controlling factor in the O-atom chemistry of Teflon and Kel-F[ref 22,23]. The EOIM-III payload received a larger VUV radiation dose than STS-8 as a result of the solar inertial hold period following deployment of the Eureca satellite during an earlier portion of the STS-46 mission.

In contrast, incorporating two CF_3 groups into a polyimide structure results in little or no change in reaction efficiency, as can be seen by comparing the reaction efficiencies of Kapton polyimide and Eymyd-F. In general, the aromatic polymers displayed significantly lower reaction efficiencies than the linear straight-chain hydrocarbons, with the notable exception of the polycarbonate. The very low reaction efficiency of the poly(bistrifluoropropylphosphazene) based polymers X-221, X-222, and Eypel-F, all showing little or no evidence of reaction, confirms earlier work in ground-based test facilities[ref 24]. Eypel-F is a durable, high-temperature elastomer which may find use in spacecraft atomic oxygen environments.

Table 2 shows the temperature dependence of the polymer reaction efficiencies determined following exposure to known O-atom fluences on the EOIM-III heated trays in the flowing discharge apparatus and in the HVAB. The temperature dependence of the O-atom reaction efficiency is shown as an empirical Arrhenius activation energy, i.e., the natural logarithm of the reaction efficiency is plotted against the reciprocal of the polymer sample temperature in degrees Kelvin, and the activation energy is reported as the slope. It should be noted that atom kinetic energy appears nowhere in this expression. For all the cases examined to date, straight-line Arrhenius plots have been obtained with correlation coefficients between 0.95 and 0.99. Inspection of table 2 shows that a large decrease in the Arrhenius activation energy is obtained on going from the flowing discharge to the HVAB or orbital environments. The large decrease in activation energy is accompanied by the large increase in reaction efficiency.

TABLE 2. The effects of atom-surface collision energy on the reaction efficiency , Re, and the parameters of the empirical Arrhenius equation, Re = A x EXP(-Ea/kT$_S$), where T$_S$ is polymer surface temperature and Ea is the activation energy in eV. Re is in cm^3/atom.

POLYMER	Re, LEO	Ea, LEO	Re,HVAB	Ea,HVAB	Re, FDS	Ea, FDS
KAPTON	3.1E-24	0.02 eV	3.3E-24	0.01 eV	2 E-28	0.3 eV
MYLAR	3.8E-24	0.05 eV	--------	--------	3 E-28	0.4 eV
D4 POLYETHYLENE	3.8E-24	0.0 eV	--------	--------	2 E-27	0.2 eV
POLYETHYLENE (PE)	3.7E-24	0.0 eV	--------	--------	4 E-27	0.2 eV
KYNAR	1.2E-24	0.0 eV	--------	--------	3 E-29	0.4 eV
TEFZEL	0.9E-24	0.04 eV	--------	--------	3 E-29	0.5 eV
LCP-4100	3.2E-24	0.04 eV	--------	--------	--------	--------
XYDAR	2.9E-24	0.05 eV	--------	--------	--------	--------
CR-39	6.1E-24	0.04 eV	--------	--------	--------	--------
EYMYD-F	2.7E-24	0.03 eV	--------	--------	--------	--------
PEEK	3.4E-24	0.03 eV	--------	--------	--------	--------

O-atom kinetic energy, on impact with the polymer surface, does not appear in the Arrhenius equation. As a result, the activation energy calculated by this method can vary with O-atom kinetic energy, if atom kinetic energy is available to overcome energetic barriers to reaction as has been previously proposed[ref 13,25]. Alternately, the mechanism of reaction could change as atom-kinetic energy approaches a threshold value. Simple, semiempirical power laws or exponential functions have been shown to produce reasonable agreement with the limited data then available in the 0.065 to 5.0 eV translational energy range which suggests that a single reaction mechanism, as well as a single energetic barrier to reaction, may determine the reaction efficiency in the O-atom kinetic energy domain of interest. The question cannot be resolved without reaction efficiency data taken at several translational energies between 0.1 and 1.0 eV.

The LANL HVAB was used to obtain reaction efficiency data on Kapton polyimide at average atom kinetic energies of 0.44, 0.72, 0.79, and 2.1 eV. Velocity distribution functions and HVAB composition were measured as described in the apparatus and methods section above. The four O-atom kinetic energy distribution functions are shown in figure 15. For comparison purposes the kinetic energy distribution functions for ram-incident O atoms in LEO (average kinetic energy = 5.6 eV) and for O atoms striking a surface immersed in flowing discharge gas (average kinetic energy = 0.065 eV) are shown in figure 16.

It should be noted that the component of the kinetic energy normal to the surface plane during collision with the surface and the total O-atom kinetic energy are the same for the O-atom directed beam on-orbit and in the HVAB. In the case of the thermalized gas in the flowing discharge, the component of the kinetic energy which is normal to the surface plane during collision with the surface and the total O-atom kinetic energy are not the same. The total kinetic energy distrubution on surface collision in the flowing discharge shown in figure 16 was calculated using well known molecular

effusion beam methods. The component of the total kinetic energy normal to the surface plane is often used in surface reactive scattering experiments on surfaces having well defined surface structures[ref 27]. The total kinetic energy on surface collision is probably more appropriate in the case of polymer films which are expected to be rough on a molecular scale and show no preferred orientation of chemical bonds.

The measured reaction efficiency of Kapton polyimide is plotted against the first moment (average value) of the kinetic energy distributions described in the previous paragraph (figures 15 and 16) in figure 17. A rapid increase in reaction efficiency is seen between 0.065 and 1.0 eV followed by relatively little change between 1.0 and 5.6 eV. The data shown in figure 17 suggest that a the dynamics of the reaction of O-atoms with polymers may be described with a line-of-centers[ref 26], a Berckele et al[ref 27], or a microcanonical transition state[ref 28] model of the kinetic energy dependence of the reaction probability. Such models have proven highly successful in describing the translational energy dependence of a number of gas phase and surface reactive scattering processes[ref 26-29]. A simple direct fit of the data plotted in figure 17 to such a model is a gross oversimplification given the width of the velocity distribution functions. A more accurate test of the translational energy dependence hypothesis is needed.

To test the hypothesis that the simple reactive scattering models provide a reasonable description of the reaction dynamics of O atoms with polymers, we form the convolution integral of the function which describes the kinetic energy dependence of the reaction probability with the normalized kinetic energy distribution function, f(Et), as shown in the equations below and then determine if the Re vs. Et data can be fit to the resulting function. Finally, we ask if the Re equation, with parameters determined by least squares curve fitting to the HVAB data, can predict values of Re for the flowing discharge and on-orbit environments.

Line of Centers Model

$$\mathrm{Re} = \int_0^\infty A(1-\frac{Ea}{Et}) f(Et) d(Et),.$$

$$A = 5.10 \times 10^{-24} cm^3 / atom \qquad Ea = 0.62eV \qquad \Delta = 0.036 \qquad (1)$$

Beckerle-Ceyer Model

$$\mathrm{Re} = \int_0^\infty \frac{A}{1+\exp - n(Et - Ea)} \times f(Et) d(Et)$$

$$A = 3.7 \times 10^{-24} \qquad n = 10 \qquad Ea = 0.98 \qquad \Delta = 0.008 \qquad (2)$$

Re, as defined by the Re equations above, is the average of a large number of reaction efficiencies, one for each kinetic energy interval in the kinetic energy distribution function of interest. The Re equations allows us to calculate the reaction efficiency given the normalized kinetic energy distribution function, f(Et), and values for the parameters Ea, the magnitude of the energetic barrier to reaction, and A, the limiting reaction efficiency at high kinetic energies. The Δ term is the residual sum of squares error at the conclusion of the curve-fitting process.

We test the hypothesis represented by an Re equation as follows. First, because apriori values for A and Ea are not available, a gaussian least squares curve-fitting process is used with A and Ea as adjustable parameters. A, Ea, and any other adjustable parameters are varied until the Re equation gives the best fit (minimum Δ) to the Re data produced by exposing Kapton samples in the four different atom beam kinetic energy distribution functions shown in figure 16. The success of the curve-fitting operation both in terms of the reasonableness of the A and Ea values obtained and the magnitude of the sum of squares error at the end of the curve-fitting process is one test of the validity of the hypothesis. A second test involves asking how accurately an Re equation, with A and Ea values determined as described above, can predict Re values for kinetic energy distributions well outside the range of values used in the least squares process. Specifically, can an Re equation, with A and Ea determined with HVAB data, predict Re values obtained from the flowing discharge and EOIM-III experiments?

The predictions of the Re equations are plotted with the measured Re values in figure 17. Clearly, both Re equations provide a reasonably accurate description of the kinetic energy dependence of the Kapton Re for the HVAB and on-orbit data. The two models differ significantly in their ability to accurately predict the Re in the flowing discharge apparatus. The Beckerle-Ceyer model produces reasonably accurate predictions of the Kapton Re over a three order of magnitude range of O-atom kinetic energy and a four order of magnitude range in Re. Failure of the line-of-centers model to predict Re at thermal energies suggests that the potential energy surface describing the reactive collision may change in such a way that Ea varies with collision energy. Finally, it is useful to note that the Beckerle-Ceyer model, with parameters estimated for Kapton, is a useful tool for making reasonable estimates of Re for a variety of polymers in both thermal and hyperthermal O-atom environments as can be seen by comparison of the data in tables 1 and 2 with figure 17.

The results of x-ray photoelectron spectroscopic (XPS) studies of several polymers are shown in table 3 where samples exposed to the O-atom flux during EOIM-III are compared with flight controls (i.e., samples exposed to to the space vacuum during EOIM-III, but not to O-atom flux). All the polymer samples show significant increases in surface oxygen content accompanied by surface depletion of carbon. However the net disturbance of the surface atomic composition is relatively small at 10 to 15 atom percent. In contrast, infrared adsorption spectra of polymer sample films show no significant difference between the oxygen exposed samples and the controls, except a

slightly smaller absorbance value for the O-atom exposed samples which were thinner than the controls as a result of O-atom reaction. Because the XPS method has a sampling depth on the order of 0 to 50 Angstroms we can conclude that O-atom reaction processes are confined to the near surface region of the polymer with no significant reaction processes occurring at the greater depths samples by infrared spectroscopy. Typical infrared adsorbance spectra of Kapton and polyethylene which were exposed to the ram O-atom flux during EOIM-III are compared to those of the corresponding flight controls in figure 18. The small differences in absorbance peak heights are the result variability in final film thickness after pressing, not O-atom reaction effects.

Table 3. Surface composition of EOIM-III polymer films, expressed as atom percent, as determined by X-ray photoelectron spectroscopy. The surface exposed to ram atomic oxygen during EOIM-III is compared with the control sample.

	O-atom Reaction Surface					Control Surface				
Polymer	**C**	**O**	**N**	**F**	**Si**	**C**	**O**	**N**	**F**	**Si**
Kapton	64.3	23.2	5.7	0.0	6.8	79.7	13.3	5.7	0.0	1.1
Mylar	71.2	24.2	0.6	0.8	2.2	75.1	22.7	0.1	0.3	1.8
PEEK	49.3	36.1	2.4	5.2	6.9	81.0	15.9	0.6	0.4	2.2
PE	80.4	14.2	1.5	0.0	3.8	94.8	3.4	0.0	0.0	1.8
PMP	86.9	9.1	0.3	0.5	3.2	97.3	1.8	0.0	0.0	0.9

Finally, profilometry and weight-loss measurements on JSC polymer samples revealed some interesting configuration interaction effects produced by the sample holders themselves. Thin metal screens were placed in front of most polymer samples on EOIM-III to act as etch masks, helping to provide for more accurate profilometry. However, the profilometry measurements showed more surface recession near the edge of the 2.065 centimeter diameter sample holder opening and less recession near the center as shown in figure 20. The effect is probably a result of the 45 degree bevel machined into the circular sample openings in the sample holders. High-velocity oxygen atoms can scatter off the beveled surface and onto the sample, effectively increasing the O-atom flux and fluence nearest the edge of the sample holder opening.

Summary and Conclusions

Despite some minor payload timing and switching problems, the EOIM-III flight experiment achieved all of its objecitves. A well-characterized, short-term, high-fluence O-atom exposure was provided for a large number of materials, many of which had never been exposed to the atomic oxygen environment in LEO before. Detailed definition of the sample exposure history is provided in reference 1. The mass spectrometer/carousel experiment produced over 46,000 mass spectra providing detailed characterization of both the natural and induced environments. The mass

spectrometric data base will prove a valuable resource in future years for the verification of various models of rarefied gas and plasma flow around spacecraft. The gaseous reaction products of various polymer species have been determined in the LEO environment and direct reactions of ambient O^+ ions with surfaces have been observed. Finally, by combining measurements of polymer reaction efficiency ,we have determined the dependence of polymer reaction efficiency on O-atom kinetic energy in an unequivocal way. Reaction efficiency data produced in the HVAB system at several different O-atom kinetic energies were shown to be described by the Beckerle[ref 29] reactive scattering model with an energy barrier of 0.98 eV. The same equation made reasonably accurate predictions of reaction efficiencies in the LEO environment and in the laboratory flowing discharge at JSC. The activation energy for the mass removal or surface recession process, defined in terms of polymer temperature only, showed a marked decrease in magnitude as O-atom translational energy is increased, a result which is expected if O-atom kinetic energy is directly available to overcome energetic barriers to reaction.

References

1) Koontz S. L., Leger, L. J., Rickman, S. L., Cross, J. B., Hakes, C. L., Bui, D. T.; "The Evaluation of Oxygen Interactions with Materials III (EOIM-III) Mission and Induced Environments," Proceedings of the Third LDEF Post-Retrieval Symposium, Williamsburg, VA, November 8-12, 1993, NASA CP-3275.

2) Jursa, A. S., editor; Handbook of Geophysics and the Space Environment, Air Force Geophysics Laboratory, United States Air Force, 1985 (National Technical Information Service).

3) Hedin, A. E., "A Revised Thermospheric Model Based on Mass Spectrometer and Incoherent Scatter Data: MSIS-83," J. Geophys. Res., Vol. 88, No. 10, pp 170-188, 1983.

4) Leger, L. J., Visentine, J. T., Santos-Mason, B.; "Selected Materials Issues Associated with Space Station Freedom," in the SAMPE Quarterly, Vol. 18, No. 2, pp 48-54, Jan. 1987.

5) Koontz, S., King, G., Dunnet, A., Kirkendahl, T., Linton, R., Vaughn, J.; "The ISAC Atomic Oxygen Flight Experiment," J. Spacecraft., in press, 1994.

6) Visentine, J. T., Leger, L. J.; "Materials Interactions with the Low-Earth Orbit Environment: Accurate Reaction Rate Measurements," AIAA paper AIAA 85-7019, AIAA Shuttle Environments and Operations II Conference, Nov. 1985, p 168.

7) Leger, L. J., Visentine, J. T., Schleising, J. A.; "A Consideration of Atomic Oxygen Interactions with Space Station," AIAA-85-0476, AIAA 23rd Aerospace Sciences Meeting, Jan. 14-17, 1985, Reno, Nevada.

8) Hunton, D. E., Trzcinski, E., Wlodyka, L., Federico, G., Dorian, J. 1Lt, USAF; "Quadrupole Ion-Neutral Mass Spectrometer for Space Shuttle Applications," AFGL-TR-86-0084, Environmental Engineering Paper No. 953.

9) Koontz, S. L., Cross, J. B., Lan, E.; "Characterization and Calibration of the EOIM-III Flight Mass Spectrometer in a High Velocity Atom Beam," in Materials Degradation in Low-Earth Orbit (LEO), Srinivasan, V., Banks, B. A., eds., The Materials, Metals and Minerals Society, 1990.

10) Visentine, J. T., comp.; NASA Technical Memorandum 100459, "Atomic Oxygen Effects Measurements for Shuttle Missions STS-8 and STS-41G: Vol. I-III," Sept. 1988.

11) Hayden, L. J., Nier, A. O., French, J. B., Reid, N. M., and Ducket R. J.; "The Charateristics of an Open Source Mass Spectrometer Under Conditions Simulation Upper Atmosphere Flight," Int. J. Mass Spectrom. Ion Phys. 15, pp 37-47, 1974.

12) Koontz, S. L., Albyn, K., Leger, L. J.; "Atomic Oxygen Testing with Thermal Atom Systems: A Critical Evaluation," J. Spacecraft, Vol. 28, No. 3, pp 315-323, May-June, 1991.

13) Koontz, S. L., Albyn, K., Leger, L.; "Materials Selection for Long Life in Low Earth Orbit," Journal of the IES, March/April 1990, pp 50-59.

14) Clyne M. A. A., Nip, W. S.; "Generation and Measurement of Atom and Radical Concentrations in Flow Systems," in Reactive Intermediates in the Gas Phase, Setzer, D. W., Editor, Academic Press, New York, pp 1-57, 1979.

15) Huie, R. E., Herron, J. T.; "Reactions of Atomic Oxygen (O^3P) with Organic Compounds," Progress in Reaction Kinetics, Vol.8, No. 1, pp1-80, 1975.

16) Koontz, S. L., Nordine, P.; "The Reaction Efficiency of Thermal Energy Oxygen Atoms with Polymeric Materials," in Materials Degradation in Low Earth Orbit (LEO), Banks, B. A., Srinivasan, V., Eds. pp 189-205, The Minerals, Metals and Materials Society, Warrendale Penn., 1990.

17) Cross, J. B., Blais, N. C.; "High Energy/Intensity CW Atomic Oxygen Beam Source," Progress in Aeronautics and Astronautics, Vol. 116, pp 143-155, American Institute of Aeronautics and Astronautics, Washington, DC, 1989,

18) Cross J., B., Koontz, S. L., Gregory, J. C., Edgell, M. J.; "Hyperthermal Atomic Oxygen Reactions with Kapton and Polyethylene," in Materials Degradation in Low Earth Orbit (LEO), Banks, B. A., Srinivasan, V., Eds. pp 1-13, The Minerals, Metals and Materials Society, Warrendale Penn., 1990.

19) Fergeson, E. E., Feshenfeld, F. C., Schmeltenkoph, A. L.; Flowing Afterglow Measurements," in Advances in Atomic and Molecular Physics, Vol.5, pp 12-13, Academic Press, New York, 1969.

20) Visentine, J. T., Leger, L. J., Kuminecz, J. F., Spiker, I. K.; "STS-8 Atomic Oxygen Effects Experiment, " AIAA paper AIAA-85-0415, 23rd Aerospace Sciences Meeting, Jan. 14-17, 1985, Reno, Nevada.

21) Personal communication, Professor John Gregory, Chemistry Department,University of Alabama, Huntsville, Alabama.

22) Koontz, S. L., Leger, L. J., Albyn, K. A., and Cross, J.; "Ultraviolet Radiation/ Atomic Oxygen Synergism in Materials Reactivity," J. Spacecraft, Vol. 27, No. 5, pp 346-348, May-June 1990.

23) Steigman, A. E., Brinza, D. E., Anderson, M. S., Minton, T. K., Laue, E. G., Liang, R. H.; "An Investigation of the Degradation of Fluorinated Ethylene Propylene (FEP) Copolymer Thermal Blanketing Materials Aboard LDEF and in the Laboratory," JPL publication 91-10, May 15, 1991, Jet Propulsion Laboratory, Pasadena, California.

24) Fewell, L., Fenney, L.; Polymer Comm., Vol. 32, No. 13, pp 393-396, 1991.

25) Arnold, G. S.; Peplinski, D. R.; Cascarano, F. M.; "Translational Energy Dependence of the Reaction of atomic Oxygen wtih Polyimide Films," J. Spacecraft, 24(5), pp 454-458, 1987.

26) Berkerle, J.D.; Johnson, A.D.; Yang Q. Y.; Ceyer, S. T. "Collision Induced Dissociative Chemisorption of CH4 on Ni: The Mechanism for Chemistry With a Hammer," J. Chem. Phys., 91(9), pp 5756-5777, 1989.

27) Stienfeld, J. I.; Francisco, J. S.; Hase, W. L. Chemical Kinetics and Dynamics, Chapter 8, "Dynamics of Bimolecular Collisions," Printice Hall, New Jersey, 1989.

28) Zeiri, Y.; Lucchese, R. R. "Collision of hyperthermal atoms with an absorbate covered solid surface II: Collision induced desorption," Surface Science, 264, pp 197-206, 1992.

29) Gonzalez Urena, A, "Influence of Translational Energy upon Reactive Scattering Cross Section: Neutral-Neutral Collisions," in Advances in Chemical Physics, Prigogine, I and Rice S. A. Eds. Vol. LXVI, John Wiley and Sons, New York, 1987, pp 231-335.

30) Swenson, G. R., Meyerott, R. E.; "Spacecraft Ram Cloud Exchange and N_2 LBH Glow," Geophys. Res. Lett., 15, 2, pp245-248, March 1988.

31) Hanson, W. B., Sanatani, S., Hoffman, J. H.; "Ion Sputtering from Satellite Surfaces," J. Geophys. Res., 86, A13, pp 11,350-11,356, Dec. 1981.

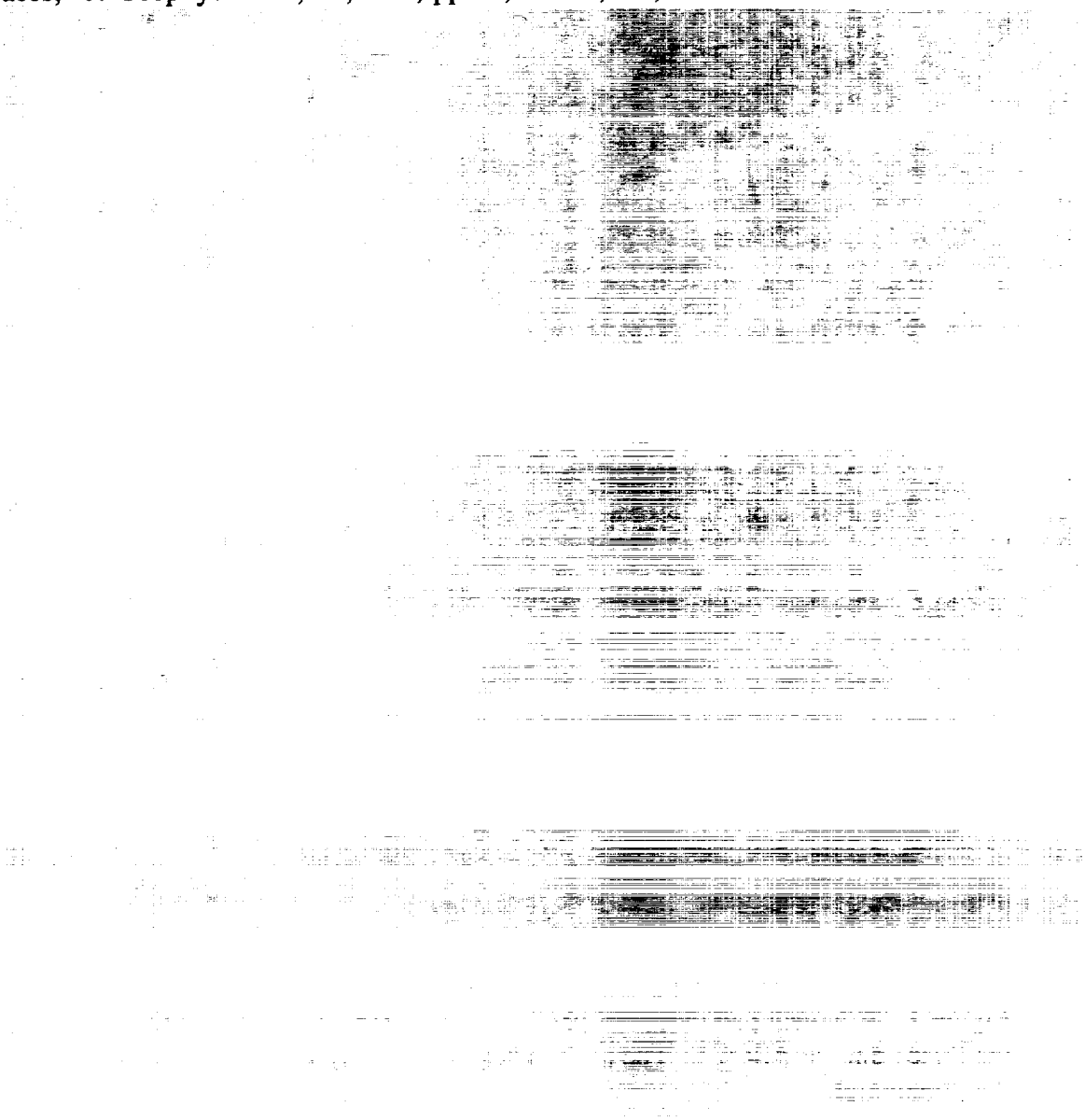

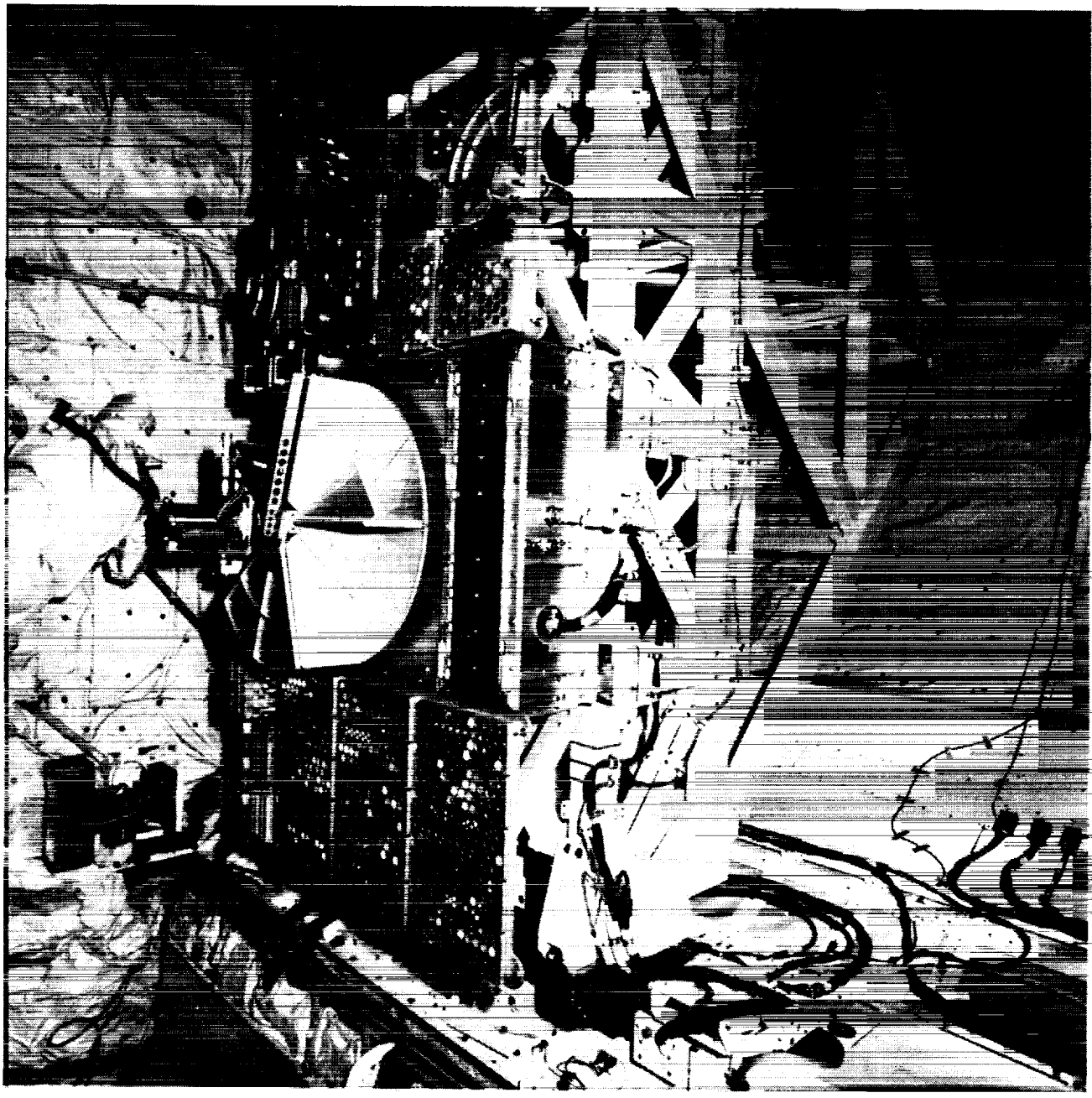

Figure 1: A launch pad close-out photo of the EOIM-III payload in the cargo bay of the Space Shuttle Atlantis. The aft bulkhead of the cargo bay is visible at the bottom of the photograph.

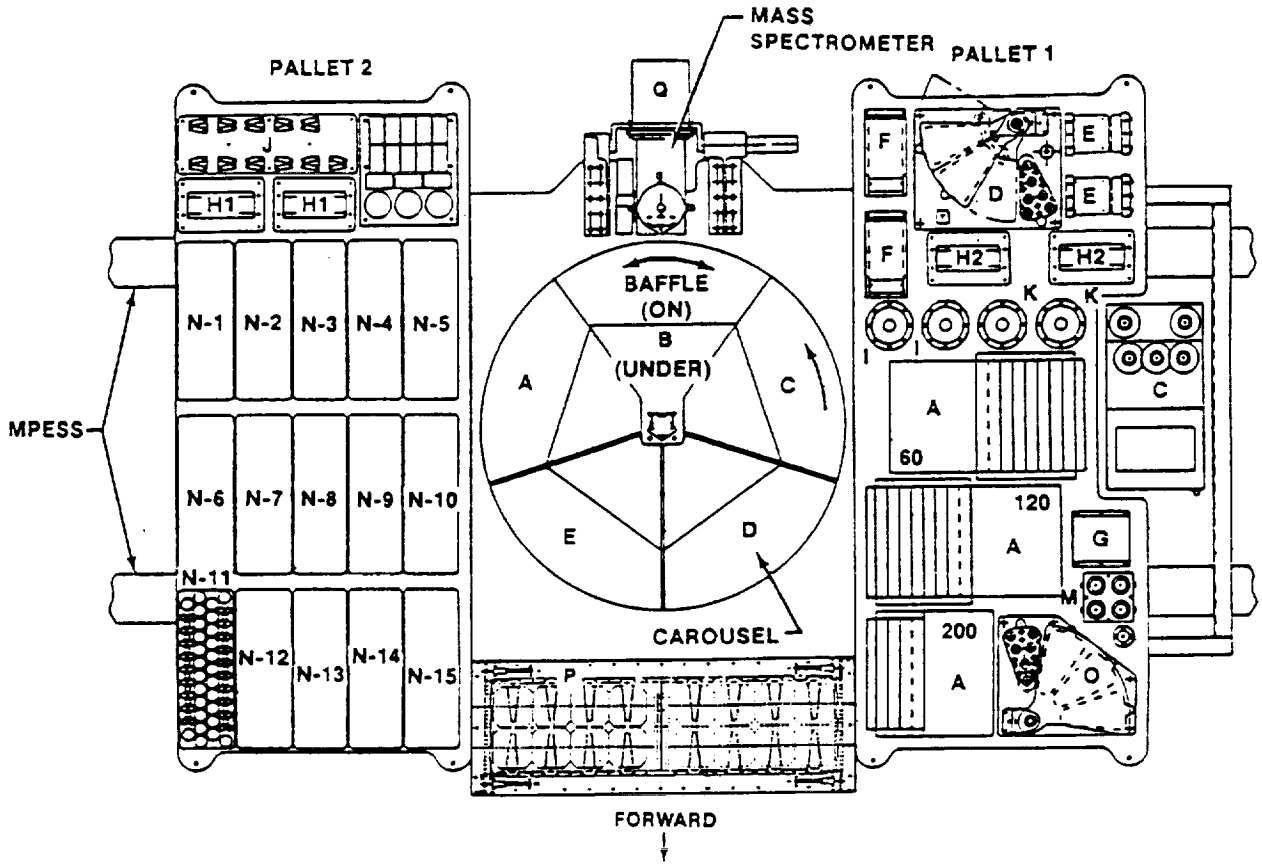

ATOMIC INTERACTION EXPERIMENTS:

A - HEATED PLATE (JSC), 3EA
B - ATOM SCATTERING EXPERIMENT (UAH), 1EA
C - ENVIRONMENT MONITOR PACKAGE (GSFC), 1EA
D - SOLAR UV EXPERIMENT (JSC), 1EA
E - STATIC STRESS FIXTURE (MSFC), 2 EA
F - UNIFORM STRESS FIXTURE (MSFC), 2 EA
G - ATOMIC OXYGEN MONITOR (MSFC), 1 EA
H1 - COMPOSITE STRESS FIXTURE(LaRC), 2EA
H2 - COMPOSITE STRESS FIXTURE (JSC), 2 EA
I - SCATTEROMETER (JPL), 2 EA
J - MECHANICAL STRESS FIXTURE (LeRC), 11 EA
K - REFLECTOMETER (LeRC), 2 EA
L - PINHOLE CAMERA (LeRC), 1 EA
M - SCATTEROMETER (AEROSPACE CORP.), 1EA
N - PASSIVE SAMPLE CARRIERS, 15 EA
O - VARIABLE EXPOSURE TRAY, 1EA
P - FREEDOM ARRAY MATERIALS EXPOSURE EXPERIMENT(LeRC), 1 EA
Q - QUADRUPLE MASS SPECTROMETER, 1 EA

Figure 2: A line drawing of EOIM-III, as viewed from directly above, showing the identification of various sub-experiments and assemblies.

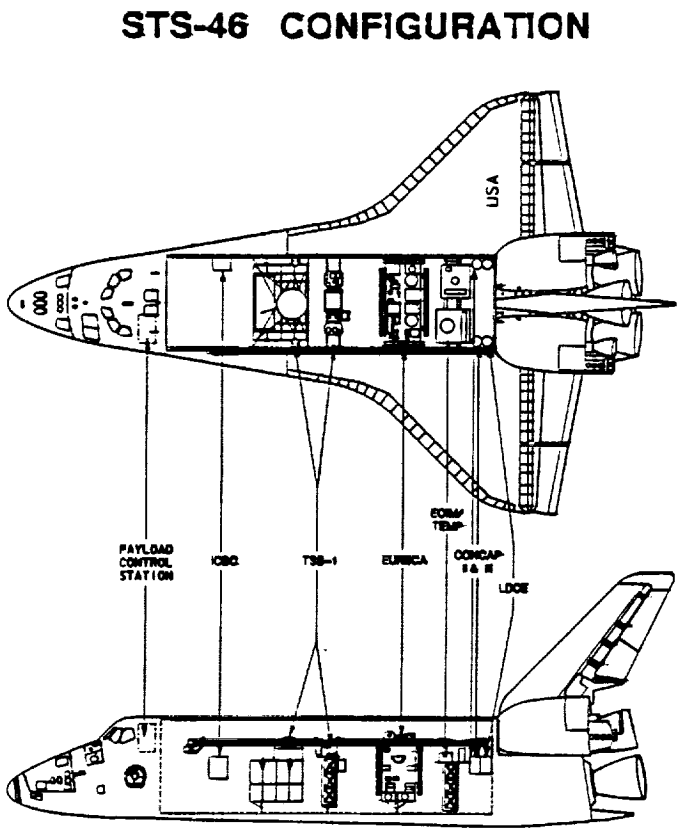

Figure 3: Cargo bay configuration for STS-46.

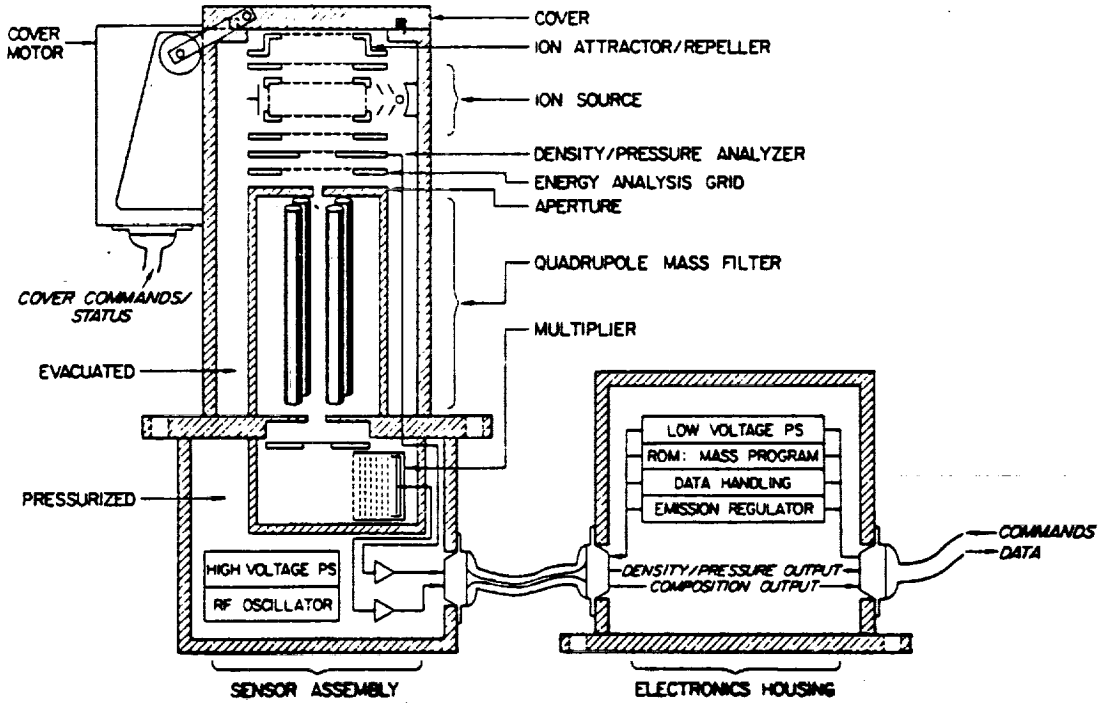

Figure 4: A cross sectional drawing of the EOIM-III mass spectrometer.

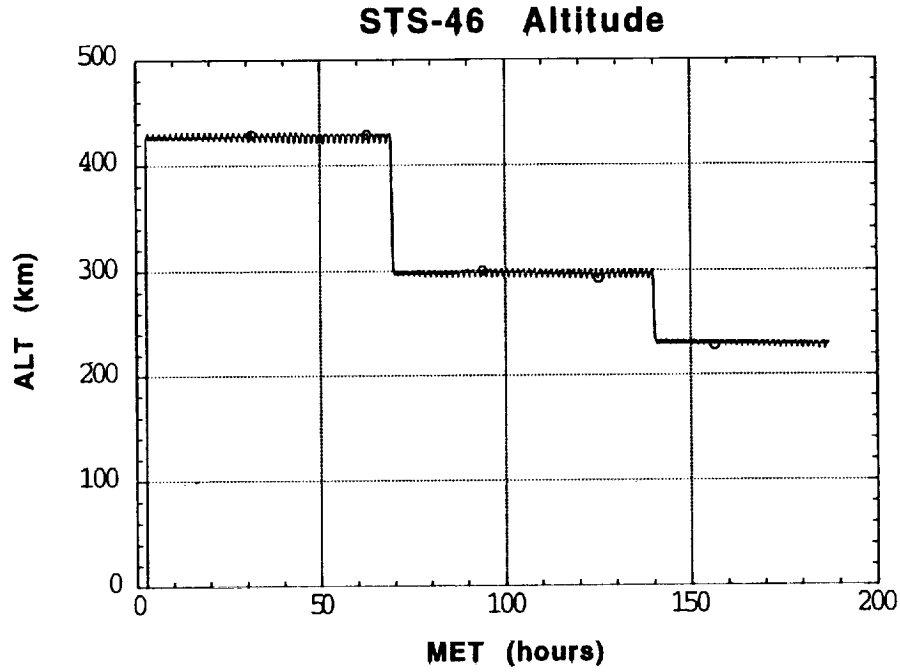

Figure 5: The altitude history of STS-46 as determined by post-flight analysis of tracking and pointing data.

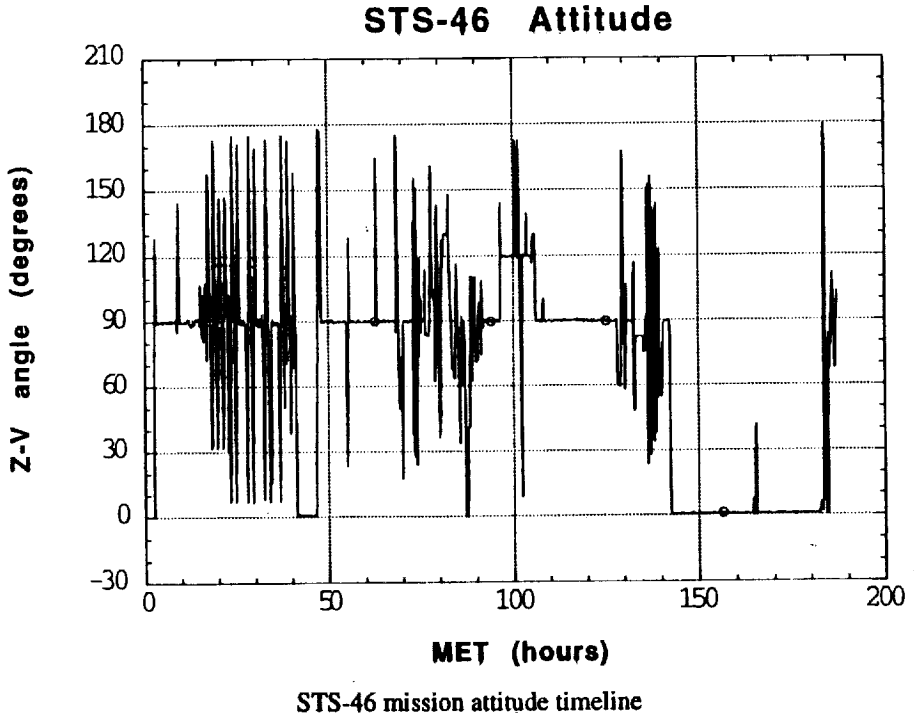

Figure 6: The vehicle attitude history of STS-46 as determined by post-flight analysis of tracking and pointing data. The attitude variable of interest for atomic oxygen fluence calculations, the angle between the cargo bay verticle (-Z) and the velocity vector (V), is shown here.

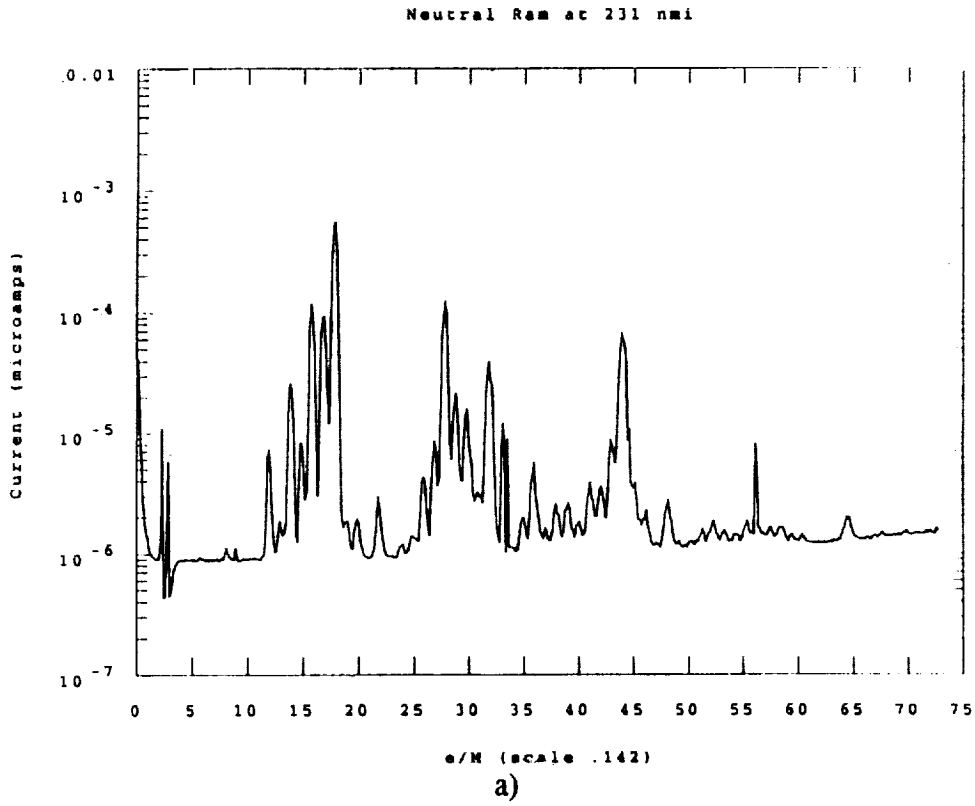

a)

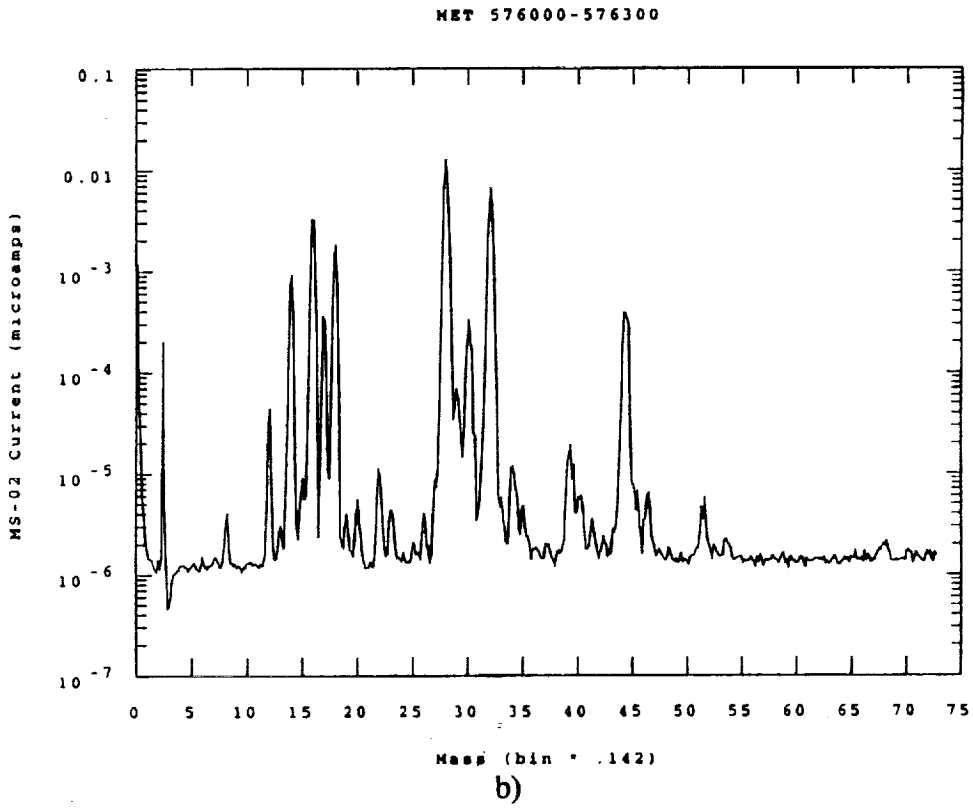

b)

Figure 7: Typical mass spectra produced with both the mass spectrometer axis and the space shuttle -Z axis aligned with the velocity vector (i.e., ram oriented). a) altitude= 231 nmi, b) altitude=123 nmi.

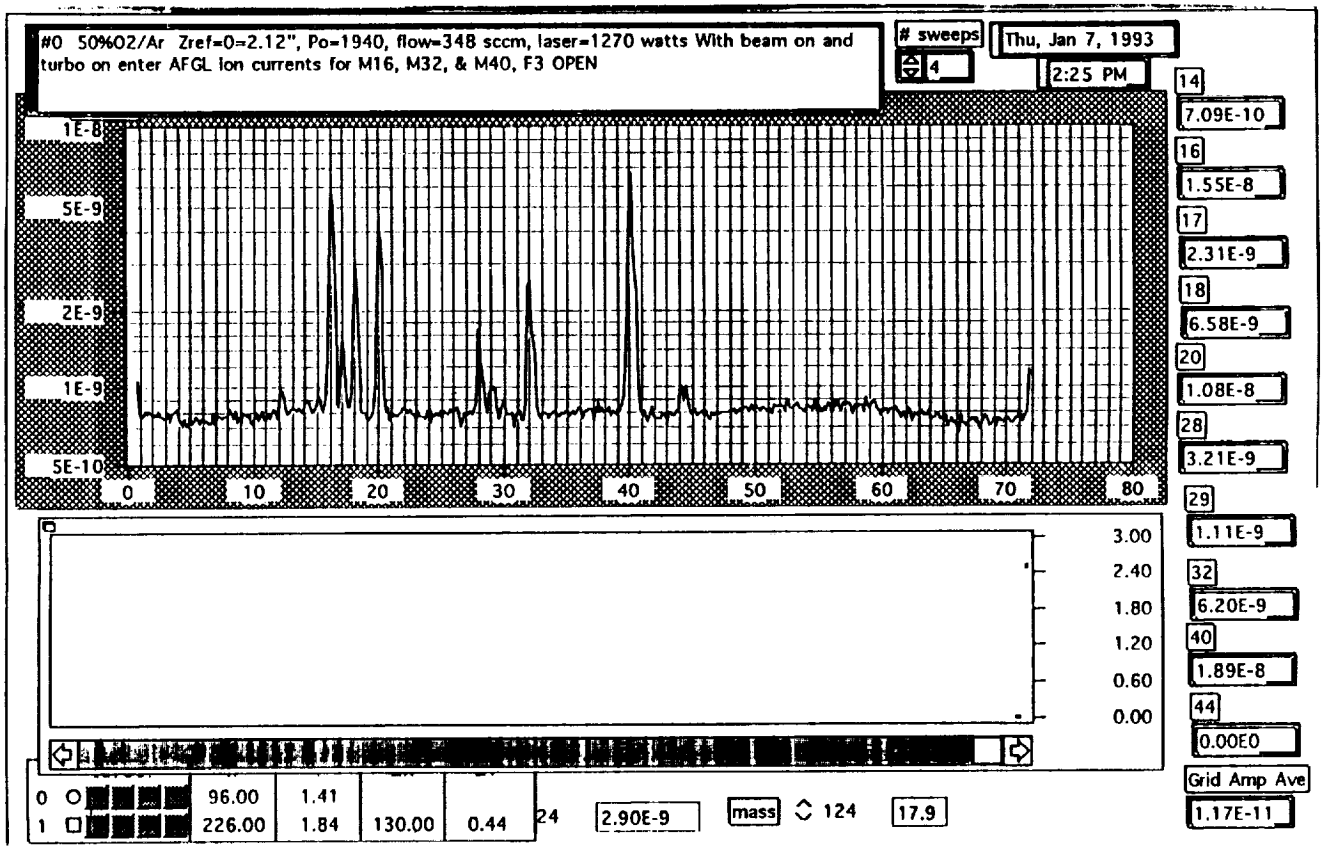

Figure 8: Typical calibration mass spectra produced by the EOIM-III mass spectrometer in the HVAB at LANL. The O-atom flux was 3.9 x 10^{15} atoms/cm^2 sec. and the argon atom flux was 4.1 x 10^{15} atoms/cm^2 sec. The O-atom kinetic energy was 2 eV.

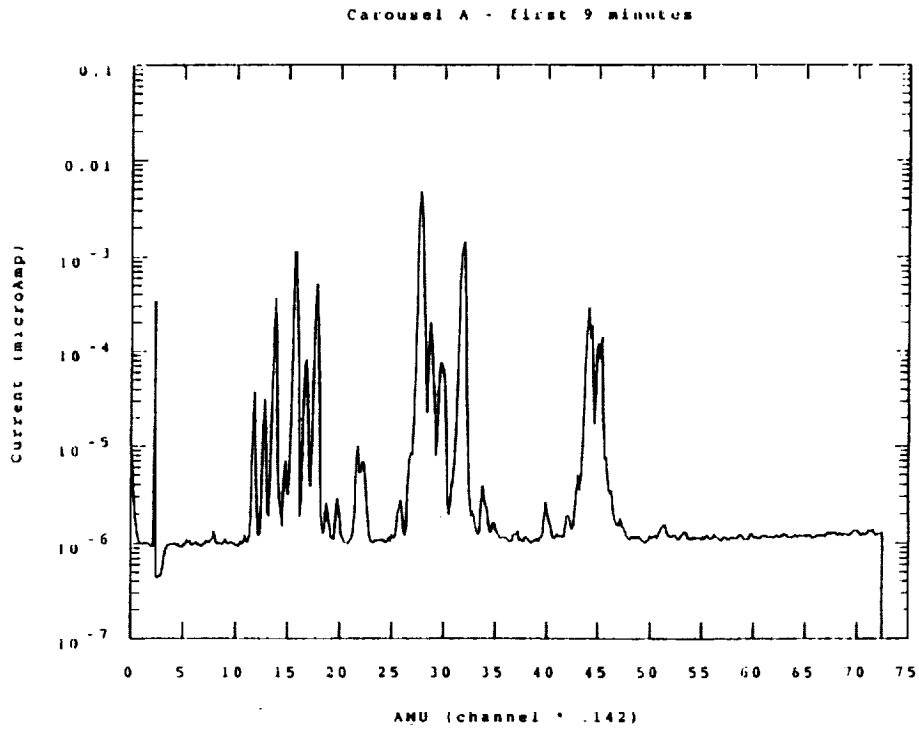

Figure 9: A typical mass spectrum of the induced neutral gaseous environment in the C^{13} labled Kapton carousel sector. The sector was open to direct ram ambient atmosphere.

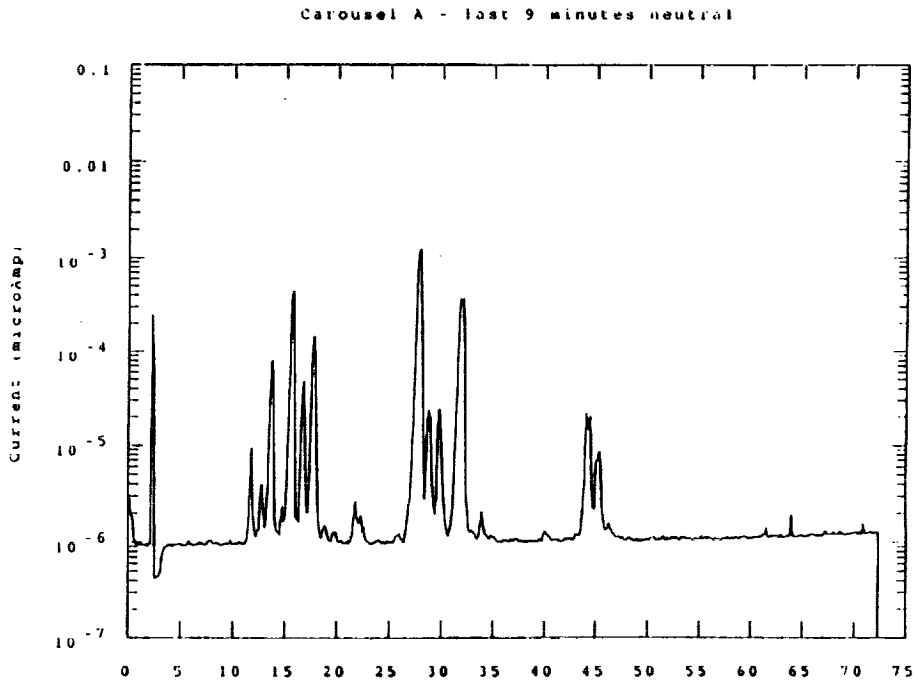

Figure 10: A typical mass spectrum of the induced gaseous environment in the C^{13} labled Kapton carousel sector. The sector cover blocked direct ram ambient atmosphere in this case.

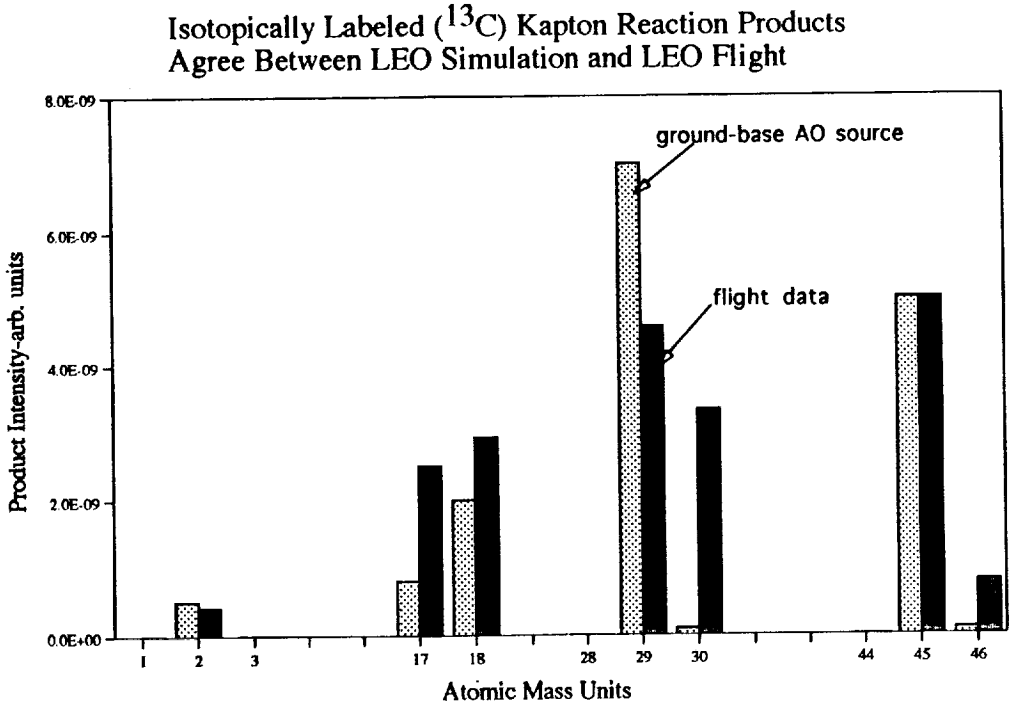

Figure 11: A comparison of the gaseous reaction products formed by O-atom reaction with C^{13} labled Kapton on-orbit and in the HVAB at LANL.

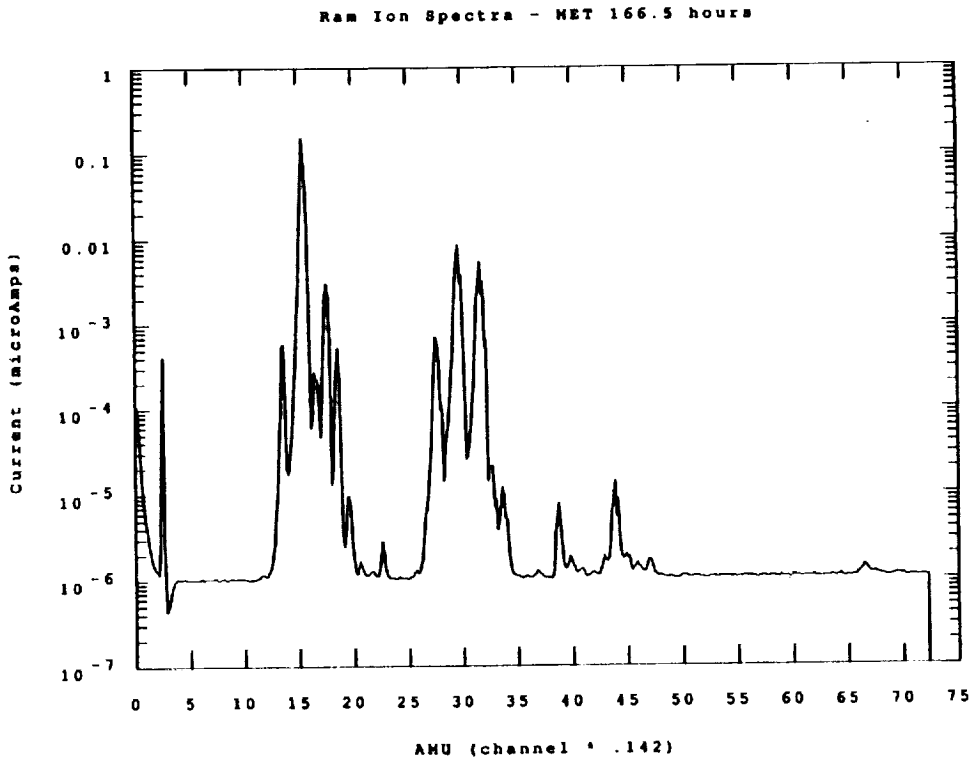

Figure 12: A typical mass spectrum of the natural ionospheric plasma environment at 123 nmi taken with the mass spectrometer configured to sample naturally occurring ionic species.

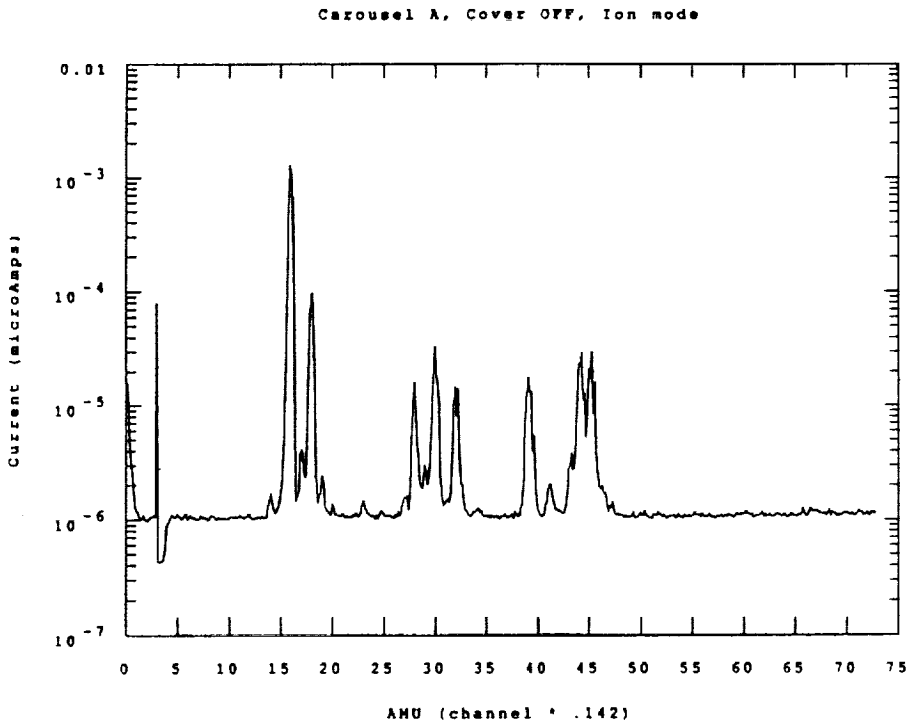

Figure 13: A typical mass spectrum of the induced plasma environment in the C^{13} labled Kapton carousel sector. The sector cover was open to direct ram ambient atmosphere.

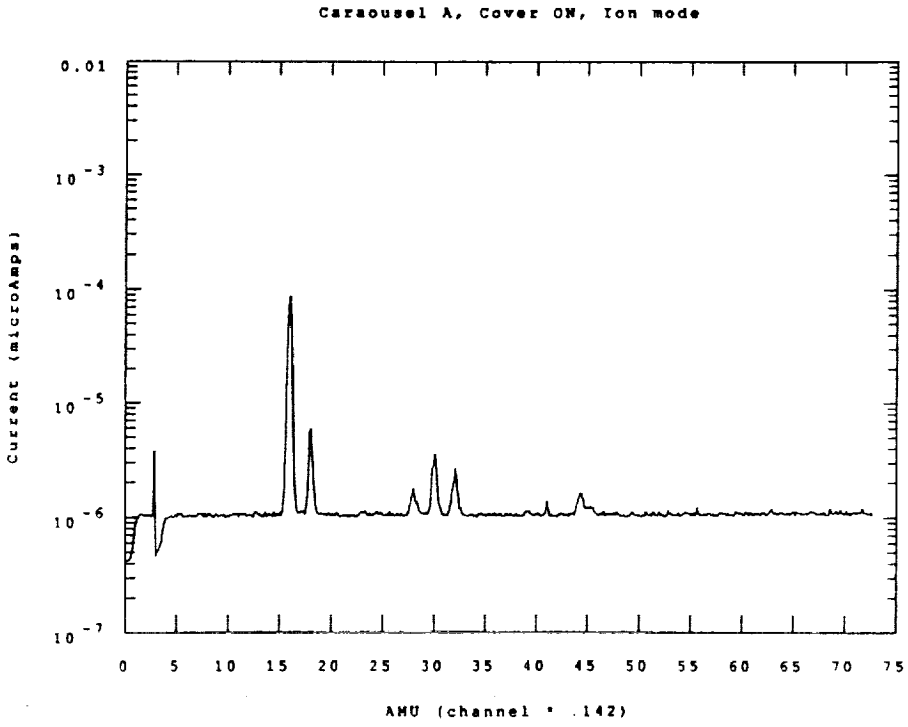

Figure 14: A typical mass spectrum of the induced plasma environment in the C^{13} labeled Kapton carousel sector. The sector cover blocked direct ram ambient atmosphere in this case.

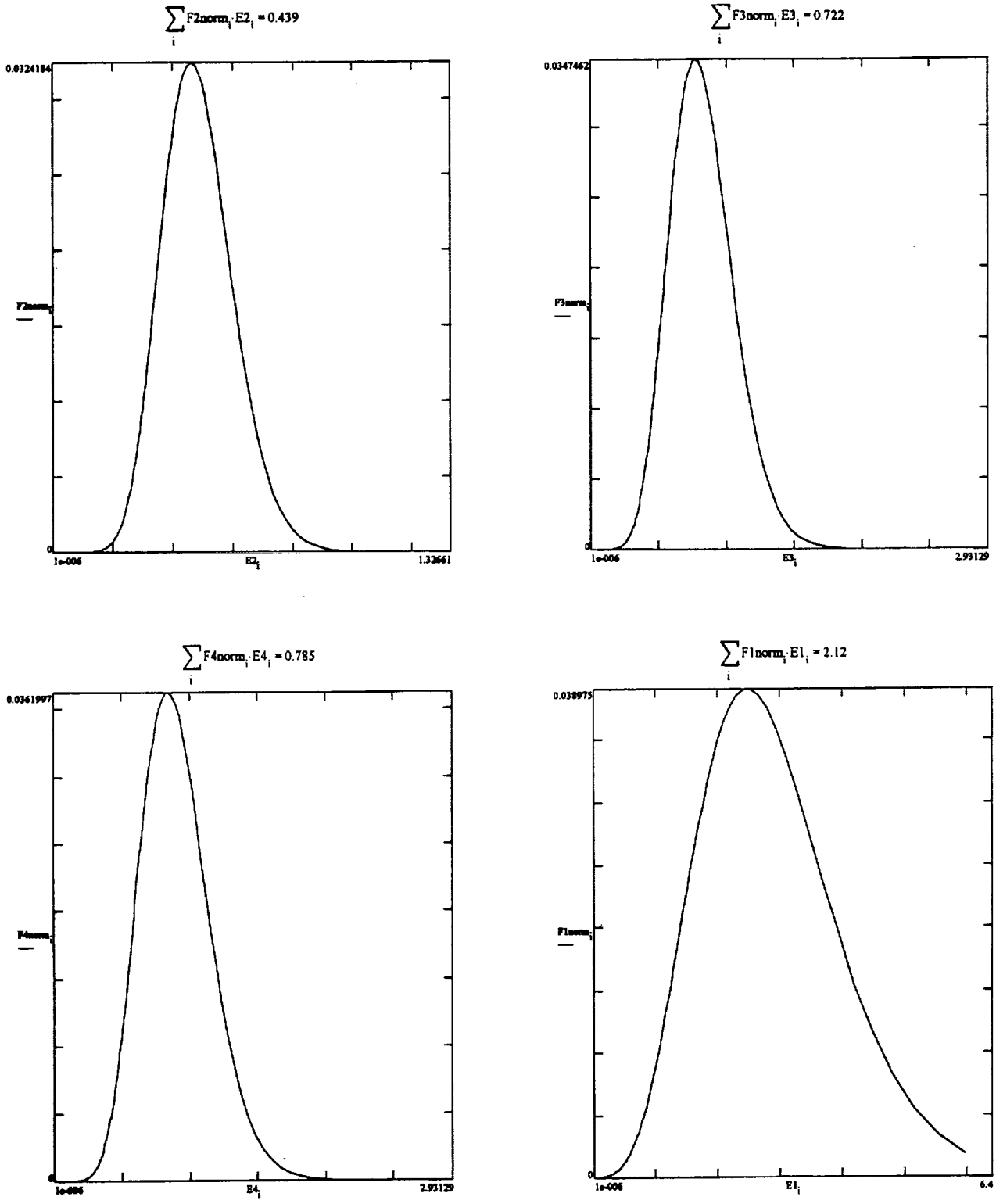

Figure 15: O-atom kinetic energy distribution functions (kinetic energy on collision with the polymer surface) and the corresponding average kinetic energies (first moments) for the HVAB O-atom beams used in developing the formula relating reaction efficiency to atom kinetic energy in eV.

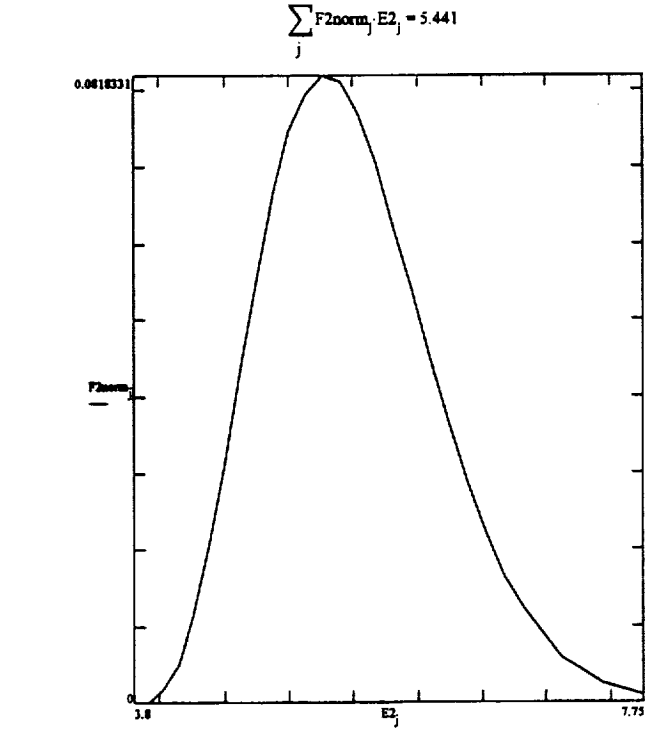

a)

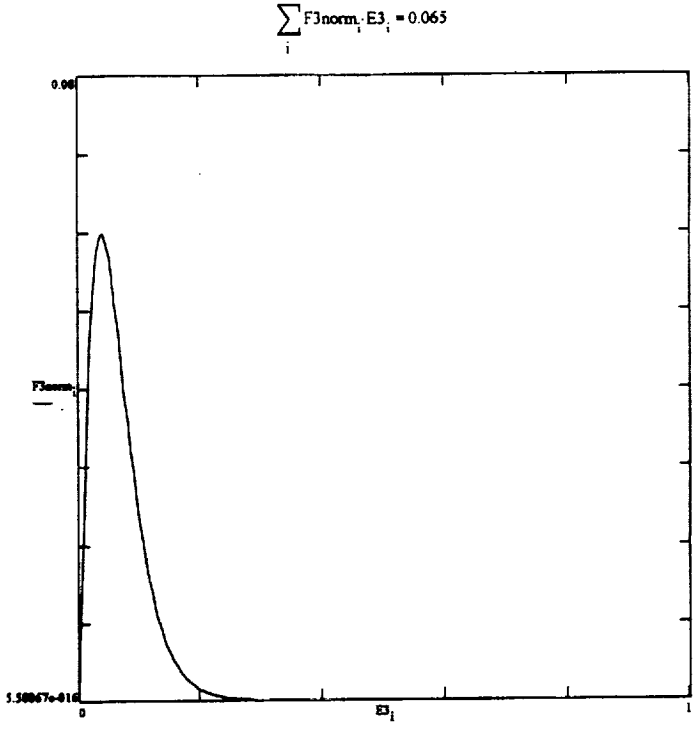

b)

Figure 16: O-atom kinetic energy (kinetic energy on collision with the polymer surface) distribution functions for, a) the LEO environment and b) the flowing discharge Energy in eV.

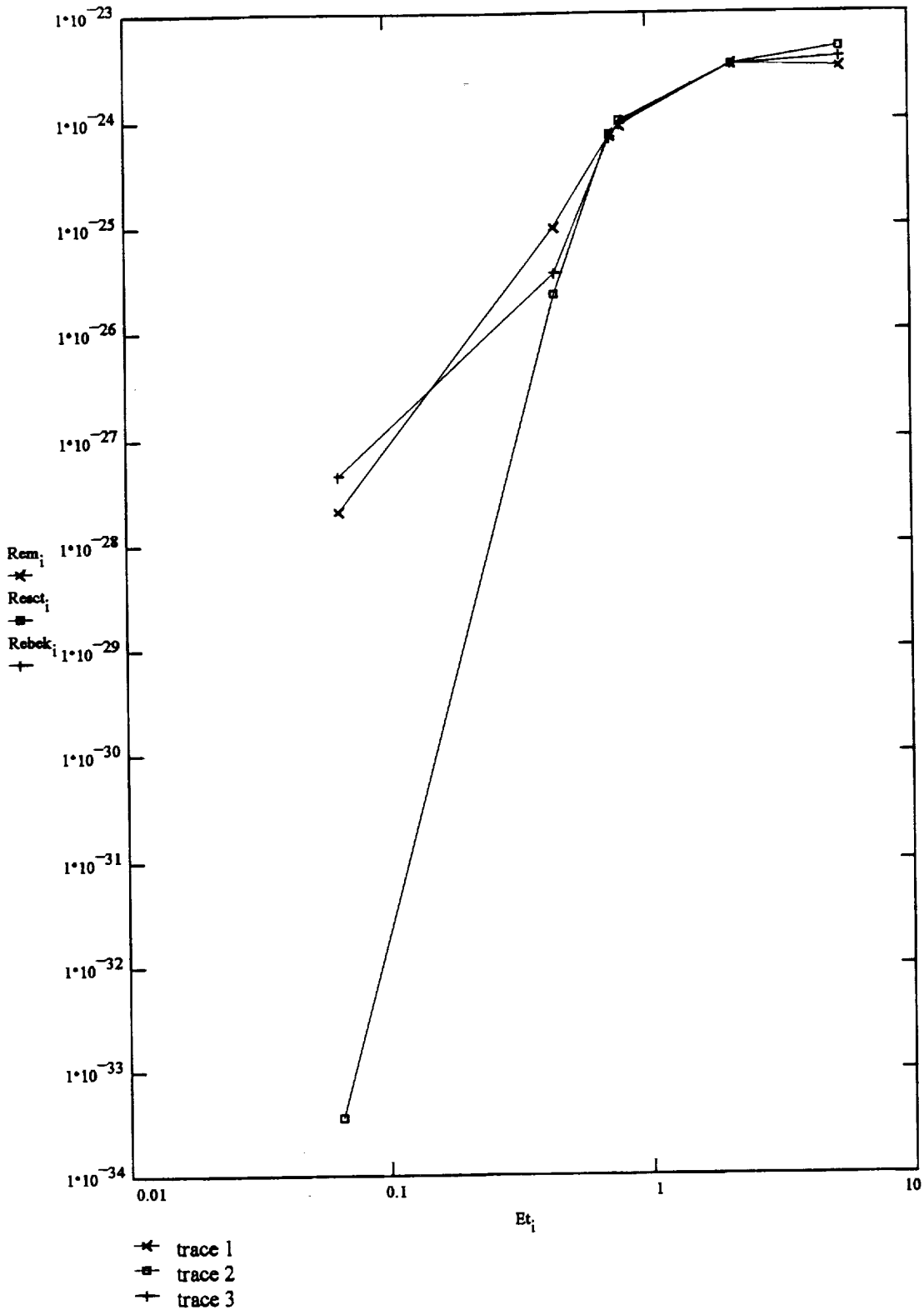

Figure 17: The measured and predicted (equations 1-3) Re values for Kapton polyimide plotted against the average value of the O-atom kinetic energy on collision with the polymer surface for the environments of figures 18 and 19: Rem = measured values, Resct = line-of-centers model, Rebek = Beckerle-Ceyer model.

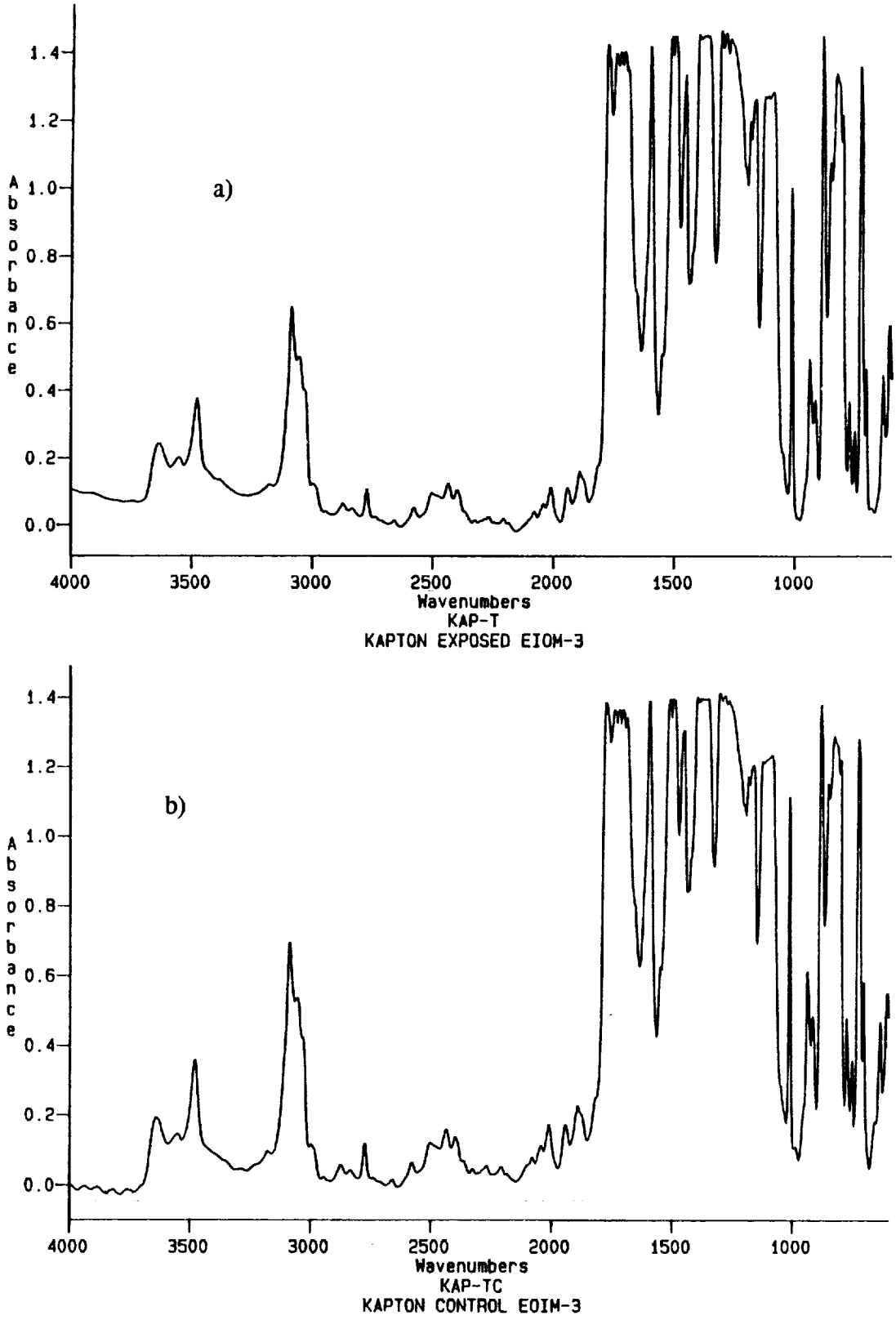

Figure 18: Typical infrared absorbance spectra of Kapton and polyethylene from EOIM-III: a) Kapton exposed to O atoms during EOIM-III, b) Kapton control, c) Polyethylene exposed to O atoms during EOIM-III, d) polyethylene control.

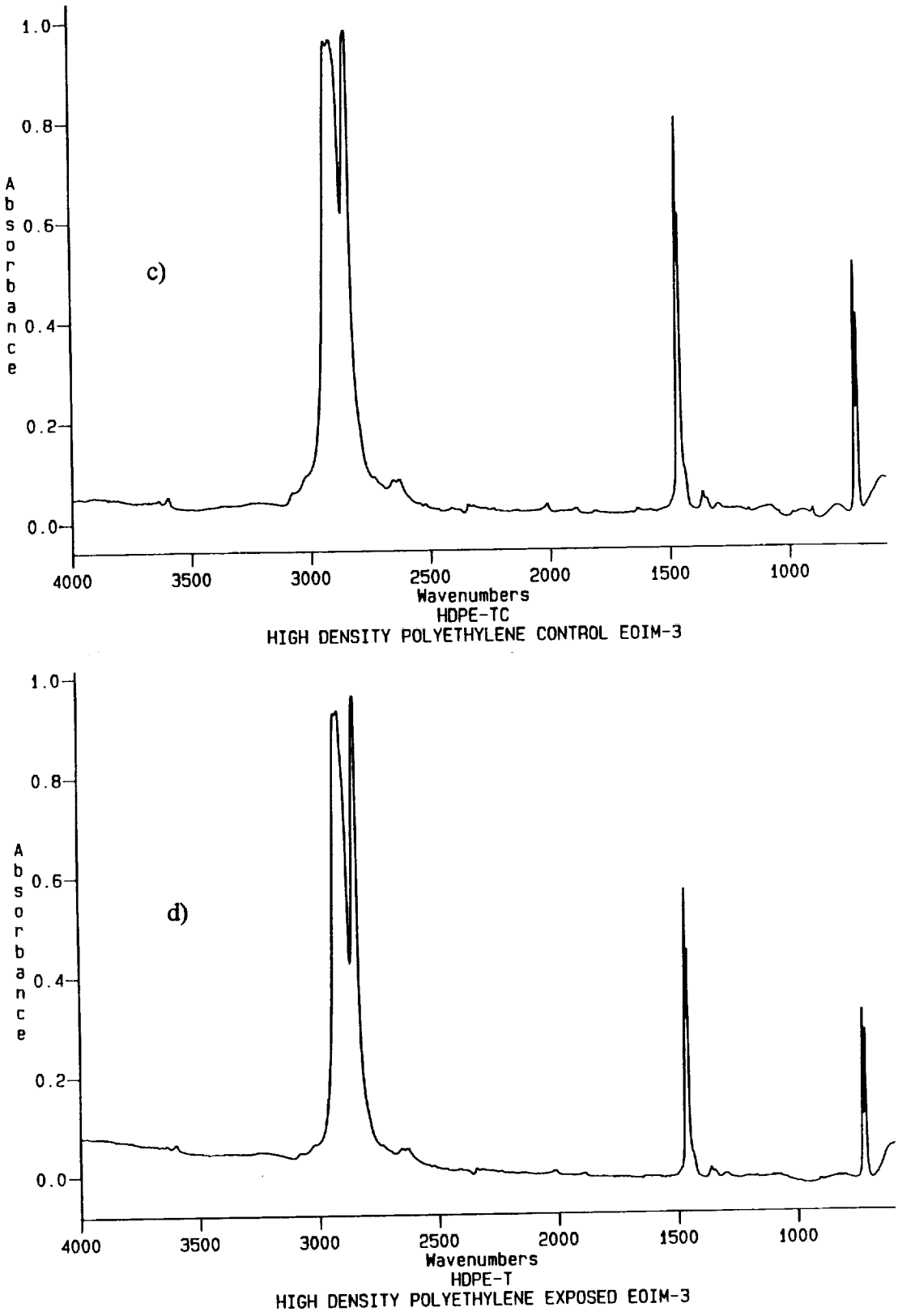

Figure 18: Typical infrared absorbance spectra of Kapton and polyethylene from EOIM-III: a) Kapton exposed to O atoms during EOIM-III, b) Kapton control, c) Polyethylene exposed to O atoms during EOIM-III, d) polyethylene control.

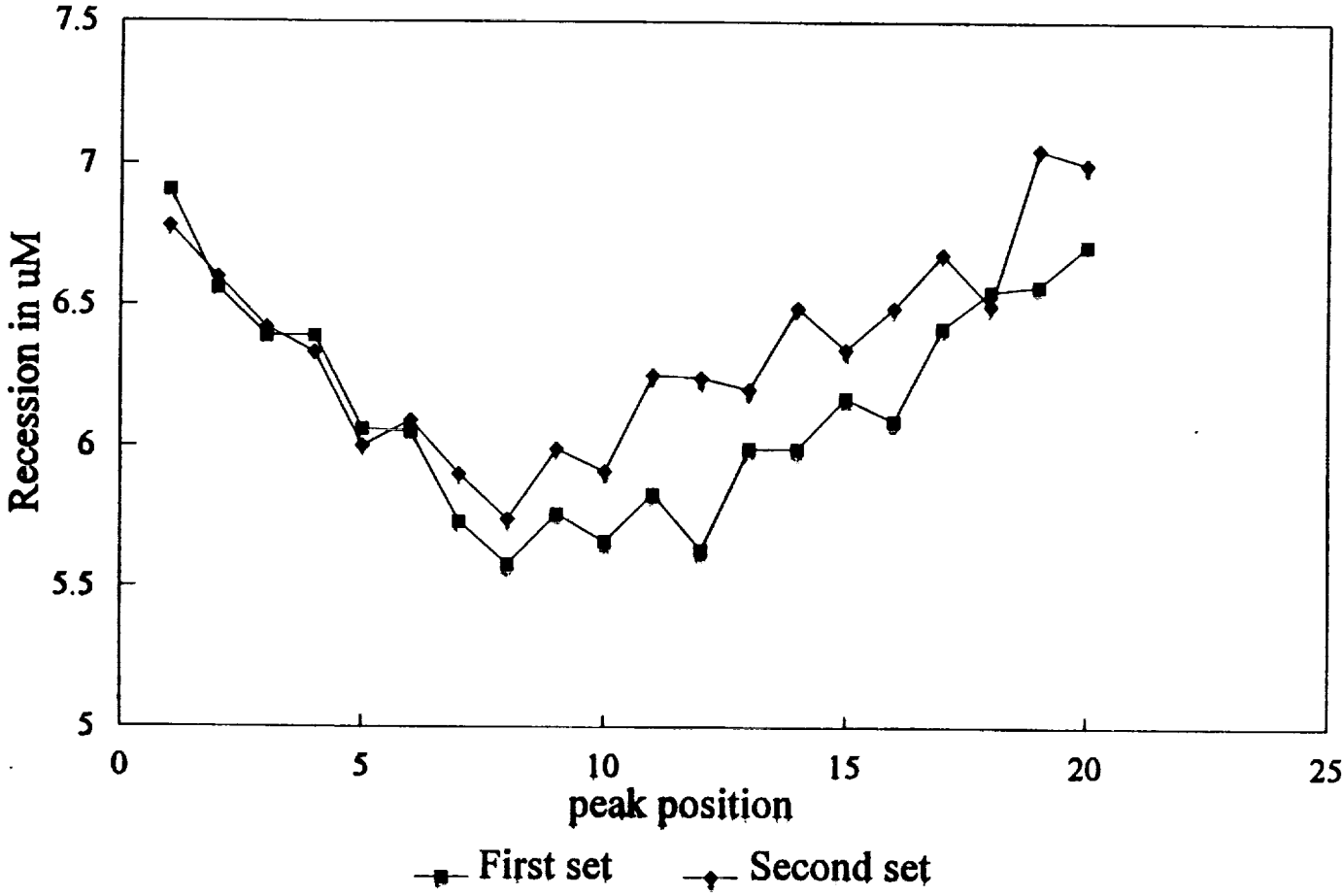

Figure 19: Configuration interaction between sample holders and ram O atoms revealed by profilometry of Kapton film specimens covered with a high transparency metal grid etch mask. Measured recession increases on moving toward the edge from the center of the sample as a result of atom scattering from the 45 degree bevel on the sample holder opening shown in the insert.